



BERGISCHE  
UNIVERSITÄT  
WUPPERTAL



JÜLICH  
FORSCHUNGSZENTRUM

# Tomographic retrieval of atmospheric trace gases observed by GLORIA

Dissertation

zur Erlangung des Grades

Doktor der Naturwissenschaften (Dr. rer. nat.)

vorgelegt der

**Bergischen Universität  
Wuppertal**

Fachbereich C – Mathematik und Naturwissenschaften

von

**Jörg Blank**

Wuppertal 2013

Die Dissertation kann wie folgt zitiert werden:

urn:nbn:de:hbz:468-20160318-114633-8

[<http://nbn-resolving.de/urn/resolver.pl?urn=urn%3Anbn%3Ade%3Ahbz%3A468-20160318-114633-8>]

## Abstract

The *Gimballed Limb Observer for Radiance Imaging of the Atmosphere* (GLORIA) is a novel remote sensing instrument combining an imaging infrared Fourier transform spectrometer with a highly flexible gimballed mount. Spectra with a unique spatial and spectral resolution are measured with a 2-D detector array. Air masses can be observed from different directions by turning the instrument's line of sight in the gimballed frame.

In December 2011 the instrument flew for the first time on the high flying Russian M-55 Geophysica research aircraft over Kiruna (Sweden). There was a very strong and cold polar vortex with several filamentary structures at its boundary which were within the operation radius of the aircraft. This thesis focuses on the retrieval of temperature and several important trace gases from measurements obtained during the ESSenCe campaign and compares them to 3-D model calculations of the atmosphere. The results show the presence of a filamentary structure of less than 1 km vertical extent, which is only visible due to the high vertical resolution of 300 m provided by GLORIA and is not fully resolved in the comparison data.

In summer 2012, GLORIA flew on the German HALO research plane during the TACTS and ESMVal campaigns. The large range of the aircraft allowed the inclusion of multiple closed loop flight tracts during the campaign, in which GLORIA made measurements with high spatio-temporal resolution. For the first time, it was possible to test the 3-D tomographic retrieval technique on GLORIA data. This technique yields 3-D trace gas fields with good horizontal resolution in every direction and thus information on very fine structures in trace gas distributions.



## Kurzfassung

Der *Gimballed Limb Observer for Radiance Imaging of the Atmosphere* ist ein neuartiges Fernerkundungsinstrument, das ein abbildendes Fourier-Transformations-Infrarot-Spektrometer mit einer leicht beweglichen kardanischen Aufhängung vereinigt. Der 2-D Detektor erlaubt es Spektren mit einer einzigartigen räumlichen und spektralen Auflösung zu messen. Luftmassen können aus verschiedenen Richtungen aufgenommen werden indem man die Sichtlinie des Instrumentes mithilfe des Kardanrahmens ändert.

Im Dezember 2011 wurde das Messgerät zum ersten Mal auf dem hochfliegendem russischem Forschungsflugzeug M-55 Geophysica über Kiruna (Schweden) eingesetzt. Am Rand des sehr kalten und starken Polarwirbels lagen mehrere Filamente, von denen sich einige in der Reichweite des Flugzeuges befanden. Aus den Messungen der ESSenCe Kampagne wurden Werte für Temperatur und verschiedene wichtige Spurengase abgeleitet und mit 3-D Modellen der Atmosphäre verglichen. Es wird eine filamentäre Struktur mit einer vertikalen Ausdehnung von weniger als 1 km beschrieben, die nur durch die hohe vertikale Auflösung von GLORIA sichtbar wird und in den Vergleichsdaten nicht vollständig aufgelöst wird.

Während des Sommer 2012 wurde GLORIA auf dem deutschen HALO Forschungsflugzeug für die TACTS und ESMVal Kampagnen eingesetzt. Die große Reichweite dieses Flugzeuges erlaubte es mehrere geschlossene Kurven zu fliegen, in denen GLORIA mit hoher räumlich-zeitlicher Auflösung gemessen hat. Mit dieser Technik können 3-D Spurengasfelder mit guter horizontaler Auflösung abgeleitet werden, in denen sehr feine Strukturen aufgelöst werden können. In dieser Arbeit wird die 3-D Tomographie zum ersten Mal auf echte Messdaten angewandt.



# Contents

<b>1</b>	<b>Introduction</b>	<b>1</b>
<b>2</b>	<b>The GLORIA Instrument</b>	<b>5</b>
<b>3</b>	<b>The JURASSIC Forward Model and Retrieval Process</b>	<b>9</b>
3.1	Solution of Inverse Problems . . . . .	9
3.2	Regularisation . . . . .	12
3.3	Forward Model . . . . .	14
3.4	Retrieval Technique . . . . .	17
3.5	3-D Tomographic Retrievals . . . . .	17
<b>4</b>	<b>Automatic Spectral Window Selection</b>	<b>19</b>
4.1	Advanced Information Content . . . . .	21
4.2	Evaluating Selections . . . . .	21
4.3	Implementation . . . . .	25
4.4	Spectral Window Selection for the GLORIA Instrument . . . . .	26
<b>5</b>	<b>ESSenCe Campaign</b>	<b>30</b>
5.1	GLORIA Data Processing . . . . .	31
5.2	Error Estimates, A Priori and Model Data . . . . .	36
5.3	Retrieval Results and Validation . . . . .	37
5.4	Validation . . . . .	42
5.5	Chapter Summary . . . . .	49
<b>6</b>	<b>Parallel Retrievals in JURASSIC</b>	<b>51</b>
6.1	Parallelisation of JURASSIC . . . . .	52
6.2	Linear Algebra . . . . .	55
6.3	Parallel Efficiency . . . . .	57

---

6.4	Chapter Summary . . . . .	58
<b>7</b>	<b>3-D Tomographic Retrieval of an ESMVal Hexagon Flight</b>	<b>60</b>
7.1	Meteorological Situation . . . . .	61
7.2	Retrieval Setup . . . . .	64
7.3	Retrieval Results . . . . .	65
<b>8</b>	<b>Conclusion</b>	<b>78</b>
<b>A</b>	<b>List of Abbreviations</b>	<b>80</b>
<b>B</b>	<b>Mathematical Notation</b>	<b>82</b>
<b>C</b>	<b>Line-by-Line Calculations</b>	<b>83</b>
<b>D</b>	<b>Adjoint Mode</b>	<b>86</b>

# List of Figures

1.1	Rossby wave breaking . . . . .	2
2.1	Limb measurement geometry . . . . .	5
2.2	Schematic drawing of a Michelson interferometer . . . . .	6
2.3	Schematics of 3-D tomographic flight paths . . . . .	7
2.4	The GLORIA instrument mounted in the belly pod of the German High Altitude Long Range Research Aircraft . . . . .	8
4.1	Examples of crossover and mutation as used in the genetic algorithm . . . . .	25
4.2	Representative evolution of the fitness function after suc- cessful genetic optimisation . . . . .	27
4.3	Spectral band between $770\text{ cm}^{-1}$ and $1000\text{ cm}^{-1}$ , showing the selected microwindows for the full retrieval setup . . . . .	28
5.1	The Russian M-55 Geophysica high altitude research aircraft	30
5.2	Flight paths of the ESSenCe campaign . . . . .	31
5.3	Cloud indices from GLORIA measurements at tangent point locations . . . . .	34
5.4	Cross section with cloud indices from MIPAS-STR . . . . .	35
5.5	Cloud detection from MIPAS Envisat . . . . .	35
5.6	Cloud top altitude from MIPAS Envisat . . . . .	35
5.7	ESSenCe: Spectra for various heights from profile 70 . . . . .	37
5.8	ESSenCe: Retrieval results for profile 70 . . . . .	38
5.9	ESSenCe: Error analysis for profile 70 . . . . .	40
5.10	ESSenCe: Vertical resolution for profile 70 . . . . .	41
5.11	2-D cross sections of temperature and volume mixing ra- tios of retrieved species . . . . .	42

5.12	GLORIA tangent points and locations of other measurements used for validation . . . . .	44
5.13	Absolute differences of temperature between GLORIA and other instruments . . . . .	45
5.14	Absolute and relative differences of nitric acid between GLORIA and other instruments . . . . .	46
5.15	Absolute and relative differences of ozone between GLORIA and other instruments . . . . .	46
5.16	Absolute and relative differences of CFC-12 between GLORIA and other instruments . . . . .	47
5.17	Absolute and relative differences of CFC-11 between GLORIA and other instruments . . . . .	48
5.18	Comparison between MIPAS-Str and the mean GLORIA profile . . . . .	48
5.19	CLAMS 10 day backward trajectories . . . . .	49
6.1	Example of a modern NUMA system . . . . .	53
6.2	Results of automatic performance optimisation for linear algebra . . . . .	56
6.3	Analysis of parallel performance for a 3-D tomographic test case . . . . .	57
7.1	The German High Altitude and LOng range research aircraft (HALO) . . . . .	60
7.2	Overview of all TACTS/ESMVal flight paths . . . . .	61
7.3	Overview of the flight path of the TACTS flight on 12th September 2012 . . . . .	62
7.4	ECMWF absolute wind velocity . . . . .	63
7.5	ECMWF horizontal wind velocity at synoptic scale . . . . .	63
7.6	Locations of microwindows in the spectrum . . . . .	64
7.7	Cloud indices for the hexagon near Antarctica . . . . .	66
7.8	Vertical field of view of every 6th pixel of the GLORIA detector . . . . .	66
7.9	Retrieval results for 3-D tomographic retrievals . . . . .	68
7.10	Retrieval results for 3-D tomographic retrievals . . . . .	69
7.11	Absolute difference between retrieval and ECMWF temperature . . . . .	69
7.12	ESMVal hexagon: Error analysis for profile 175 . . . . .	71

---

7.13 Retrieval results for CFC-12 and comparison to CLaMS . . . . .	72
7.14 Diagnostic values for ozone . . . . .	73
7.15 Diagnostic values for nitric acid . . . . .	74
7.16 Diagnostic values for temperature . . . . .	75
7.17 Comparisons between 1-D retrievals and 3-D retrievals sampled at the tangent points . . . . .	77
D.1 Adjoint derivation for a simple function . . . . .	87

# List of Tables

4.1	Retrieval targets . . . . .	26
4.2	Selected microwindows and primary and secondary associated targets by information gain . . . . .	29
5.1	A priori data used for the retrievals . . . . .	36
5.2	Error estimates for the retrieval depending on instrument and atmospheric situation . . . . .	39
5.3	Instruments used for validation . . . . .	43
6.1	Typical memory usage for a 3-D tomographic retrieval . .	54
6.2	Runtime of the 3-D tomographic benchmark . . . . .	58
7.1	Microwindow selection for 3-D tomographic retrieval . . .	65
C.1	Values used for line-by-line calculations . . . . .	84

# 1. Introduction

The Upper Troposphere and Lower Stratosphere (UTLS) is a key region in the effort to understand the future of the Earth's climate (*Holton et al.*, 1995). The troposphere is the lowest layer in the atmosphere. Its upper regions can exchange air masses with the lower regions of the next layer, the stratosphere. The lower stratosphere, where this mixing occurs, is distinct from the upper stratosphere. The part of the stratosphere which does not take part in mixing and further layers, e.g. the mesosphere is often called the overworld. Different mixing phenomena cause an important input of various trace gases from the troposphere into the stratosphere. Events like Rossby wave breaking of the subtropical and polar jet and upwelling due to high convection are observable by limb sounding. These dynamic events take place at heights which are still accessible by research aircraft.

Of particular interest is the intrusion of air rich in water vapour into the lower stratosphere. The transport of air from the tropics into the polar regions due to the Brewer-Dobson circulation is responsible for the very low mixing ratios of water in the stratosphere. Water vapour is efficiently frozen out by the cold temperatures at the tropical tropopause. With its large spectral footprint, even small changes in its mixing ratio have a great influence on the global radiation budget. It has been shown that the increase in the water vapour mixing ratios in the UTLS has a significant influence on future ground temperatures due to down-coupling effects (*Riese et al.*, 2012).

Observations form the basis for the exploration of the Earth's atmosphere. However, all measurement methods have their constraints. For atmospheric observations, this constraint is often the spatial resolution. However, many small scale processes of particular interest in atmospheric science are very hard to measure accurately. An improvement in spatial

resolution is often gained at the expense of a deterioration in coverage. In the vertical direction, the extent of structures in atmospheric temperature or trace gas distributions is up to two magnitudes smaller than in the horizontal directions. Dynamic events, like Rossby wave breaking (Figure 1.1), often lead to mixing between stratospheric and tropospheric air masses. Prior to the mixing, turbulence forms filaments with vertical extents of only tenths or hundredths of metres (e.g. *Plumb, 1992; Bradshaw et al., 2002*). Currently there is a lack of observations with sufficient resolution and coverage to explore such filaments. Current instruments are either satellite-based remote sensing instruments, with good coverage, but insufficient resolution, or aircraft or balloon-based in situ instruments, which have a good resolution, but their measurements are limited to the platform’s flight path.

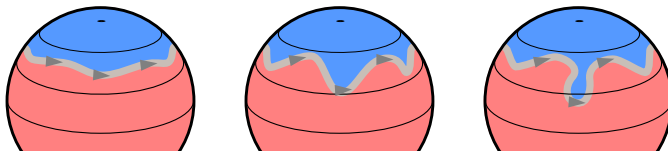


**Figure 1.1:** Meanders of the polar jet (grey band) forming under the influence of the Coriolis force (left, middle). Rossby wave is breaking and deposits cold air into the lower latitudes, initiating a mixing event (right).

A distinction is usually made between two different types of remote sensing instruments. Active remote sensing instruments illuminate their target, mostly by emitting some form of electromagnetic field, i.e. radar waves or laser light, and measure the intensity of the reflected radiation and, in some cases, the attenuation along the path. The other class of instruments works entirely passively by measuring radiation from other sources.

Remote sensing instruments can also be distinguished by their viewing geometry. Common geometries are zenith or nadir pointing, looking directly upward into the sky or downward from a satellite onto the surface. Both modes have good horizontal resolution, but very low vertical resolution at least for most passive techniques. An alternative is the limb-sounding geometry in which the instrument is pointed slightly above the horizon into the atmosphere (Figure 2.1). In nadir mode, passive instruments commonly gain some altitude information from the optical

---

thickness of different spectral lines. Passive limb sounders obtain this information from their viewing geometry.

Limb sounding is a proven technique already employed by various instruments. All the following instruments have in common that they measure the thermal emissions of the air. Some of them are mounted on satellites, which provide a stable platform with global coverage, while aircraft-based instruments focus on regions and specific meteorological conditions.

The atmosphere emits most radiation in the thermal infrared. The spectral range from 8 to 12  $\mu\text{m}$  is called the fingerprint region, because the rotational and vibrational bands of many important atmospheric trace gases are located in this spectral region. In the limb geometry, the amount of air in the line of sight is much larger than in nadir sounding. This leads to a improved reception of emissions from faint trace gases.

The infrared limb-emission observation technique was pioneered by two instruments, the Cryogenic Infrared Spectrometers and Telescopes for the Atmosphere (CRISTA) and the Michelson Interferometer for Passive Atmospheric Sounding (MIPAS) in terms of spatial and spectral resolution.

The Cryogenic Infrared Spectrometers and Telescopes for the Atmosphere (CRISTA) instrument was developed by the University of Wuppertal and was flown twice on Space Shuttle missions (*Offermann et al.*, 1999; *Grossmann et al.*, 2002). A grating spectrometer was used to measure a wide spectral range in the thermal infrared with good spectral resolution. Parts of the optical system of CRISTA were later reused by the aircraft version CRISTA-NF (*Kullmann et al.*, 2004), which participated in several aircraft campaigns (e.g. *Weigel et al.*, 2010; *Kalicinsky et al.*, 2013).

Traditionally, filamentary structures in atmospheric trace gases are investigated by using a combination of models and 1-D measurement data. Satellite data can be used to study the global structure of extended filaments (e.g. CRISTA, *Bacmeister et al.*, 1999). Recently, it was possible to resolve the 2-D structure of very fine filaments by using aircraft remote sensing data (CRISTA-NF, *Ungerermann et al.*, 2012a).

The Michelson Interferometer for Passive Atmospheric Sounding (MIPAS) is an interferometer with very high spectral resolution. Several versions of this instrument exist. The most prominent was operated on ESA's Envisat satellite (*Fischer et al.*, 2007). The balloon and aircraft-

based instruments are still in use by the Research Centre Karlsruhe (*Woiwode et al.*, 2012).

To increase the spatial resolution of airborne limb sounding, the research centres at Jülich and Karlsruhe jointly developed the Gimballed Limb Observer for Radiance Imaging of the Atmosphere (GLORIA), the first realisation of the 2-D IR limb imaging technique (*Riese et al.*, 2005). It is a Michelson interferometer with a 2-D detector array. In imaging configuration, the instrument can measure a complete vertical profile at once, with greatly increased temporal sampling. The instrument also demonstrates the infrared imaging technology for space application.

This work presents an evaluation of the first measurements by GLORIA taken during the ESA Sounder Campaign (ESSenCe, *Kaufmann et al.*, 2013) in 2011. This campaign provided the first opportunity to test GLORIA under real conditions. Sufficient data was gathered to show the viability of the instrument.

The combined campaigns Transport and Composition in the UT/LMS (TACTS, *Engel and Boenisch*, 2013) and Earth System Model Validation (ESMVal, *Schlager et al.*, 2013) provided the first opportunity to perform dedicated flight patterns to acquire GLORIA measurements for a 3-D tomographic reconstruction of atmospheric filaments. Small-scale 3-D structures can only be investigated by using models with the best resolution available. 3-D tomographic GLORIA measurements provide a new view into these structures.

The focus of this thesis is on the analysis of GLORIA data from the ESSenCe and the TACTS/ESMVal campaigns. For the data analysis, a suite of models and tools was developed to process the spectral radiance measurements of GLORIA into 3-D fields of atmospheric constituents. A short description of the GLORIA instrument is given in Chapter 2. The forward model and the retrieval processor are introduced in Chapter 3. A method to automatically select appropriate spectral features for the retrievals is described in Chapter 4. The data analysis for the ESSenCe campaign is shown in Chapter 5. For the 3-D tomographic retrievals a new parallelisation was implemented and is introduced in Chapter 6. First results from a 3-D tomographic multi-target retrieval of measurements from the TACTS/ESMVal campaigns are presented in Chapter 7. The conclusions are put forward in Chapter 8.

## 2. The GLORIA Instrument

The GLORIA instrument is a limb-sounding infrared spectrometer. This viewing geometry provides a very long path through the atmosphere, in which even faint trace gases provide a measurable signal (Fig. 2.1). This path is also called the line of sight (LOS). In contrast to nadir viewing, which looks straight down towards the earth, the line of sight leaves the atmosphere again. Infrared limb sounding is not influenced by the warm surface, but sees only cold space as a background.

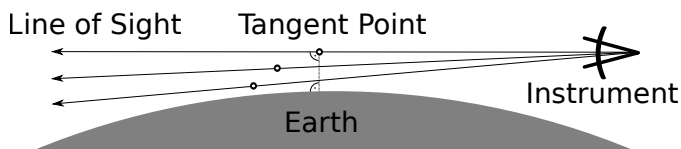


**Figure 2.1:** Limb measurement geometry. The point closest to the ground on each line of sight is called the tangent point.

The point on the line of sight that is closest to the ground is called the tangent point. The radiation emitted by the air molecules depends heavily on the number density. The method provides good vertical resolution, because the number density is proportional to the atmospheric pressure, which decreases exponentially with height. Thus the major fraction of the radiation is emitted at or near the tangent point. In limb geometry, this most important region is elongated along the line of sight, smoothing out any inhomogeneities. Its horizontal shape across the line of sight is quite small, leading to a very good spatial resolution across the measurement direction.

The optical system of GLORIA contains a Michelson interferometer for the long-wavelength infrared region between  $6 \mu\text{m}$  and  $12 \mu\text{m}$ . It uses a

high-performance 256x256 pixel MgCdTe detector in photovoltaic mode. The detector is cooled to 60 K by a Stirling cooler, the interferometer and the optic components are cooled to 210 K by solid CO<sub>2</sub> to reduce background radiation (*Friedl-Vallon et al.*, 2006).

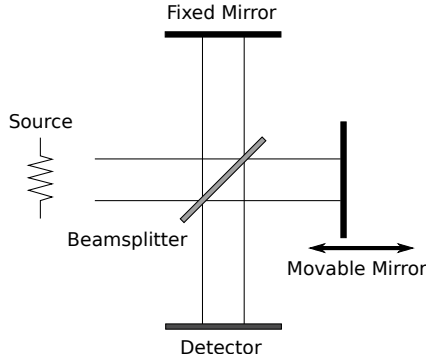


**Figure 2.2:** Schematic drawing of a Michelson interferometer. The optical path difference generated by the movable mirror creates an interference pattern on the detector.

Figure 2.2 shows a schematic drawing of the interferometer (*Michelson and Morley*, 1887). Incoming light is redirected into the two arms by a beam splitter, reflected off the mirrors and projected onto a detector after recombining. The mirror on one arm of the interferometer is movable to generate a difference in the optical path. When the mirror is moved an interference pattern is generated on the detector. This interferogram contains the spectral information of the incoming radiation. Interferometers provide two advantages in comparison to conventional grating spectrometers. The optical system allows a larger throughput (the throughput or Jacquinot advantage, *Jacquinot*, 1960), because no slit is needed and the sensor receives light from all wavelengths at the same time thus effectively increasing the signal to noise ratio (the multiplex or Fellgett advantage, *Fellgett*, 1951). By using a detector array instead of a single detector element the performance of the interferometer can be increased considerably. Instead of one interferogram, it is now possible to record a complete height profile at once (*Riese et al.*, 2005).

The instrument has a total field of view of 4° horizontally and vertically, which is projected onto a 128x128 pixel area on the detector. This

translates to an instantaneous field of view of  $0.03125^\circ$  or about 140 m at the 10 km tangent point when seen from 15 km altitude. The exact distance varies over altitude and is smallest at the instrument level and largest at the lowest tangent point. The detector rows are averaged to reduce noise.

After recovering the spectrum from the interferogram by applying a Fourier transformation (this instrument type is also called Fourier transform spectrometer or FTS), a calibration step is needed because the measurements still contain unwanted emissions, e.g. from the spectrometer body. In addition, the spectral response of the detector is not known precisely. Two black bodies are included in the instrument to provide a reference point for calibration (*Olschewski et al.*, 2012). The black bodies have a very high emissivity and are precisely temperature-controlled. Additional deep-space measurements can be used as a baseline for the instrument's self-emission. The length of the interferogram influences the spectral resolution and the time needed to take one image. There are two major modes defined for GLORIA: the chemistry mode with a high spectral resolution of  $0.0625\text{ cm}^{-1}$  and the dynamics mode with a higher spatial/temporal resolution in exchange for a spectral resolution of  $0.625\text{ cm}^{-1}$ . One dynamics mode measurement takes around 1.5 sec as opposed to 10 sec in chemistry mode. For comparison, the MIPAS-STR instrument, which is also an infrared high resolution Michelson interferometer with a single detector pixel, needs 2.8 min to record one profile of 17 altitude steps.



**Figure 2.3:** Schematics of 3-D tomographic flight paths (*Ungermaun*, 2011). Left: Closed loop circular flight pattern. Right: Linear flight path with panning.

The interferometer system itself is mounted in a gimbal frame and

is movable in all axes (Figure 2.4). The frame is used to stabilise the viewing direction even under the influence of the rather unsteady aircraft platform. It is also possible to point the instrument  $10^\circ$  upwards to take deep space measurements. However, the defining feature is the possibility of pointing the instrument from  $45^\circ$  forward to  $135^\circ$  backward. In dynamics mode, the azimuth angle is changed by  $4^\circ$  after every measurement. One step usually takes around 6 sec to record an interferogram and move the instrument. A whole cycle from back to front takes 2.5 min.

This flexibility can be used to generate measurements for 3-D tomographic retrievals (Chapter 7). An air volume can be scanned from a multitude of different angles by using a closed loop flight path around the volume and pointing the instrument inward, while scanning over the available range of angles with respect to the aircraft. When the flight path is linear, depth information along the line of sight can be gained from panning the instrument (Picture 2.3).



**Figure 2.4:** The GLORIA instrument mounted in the belly pod of the German High Altitude Long Range Research Aircraft.

# 3. The JURASSIC Forward Model and Retrieval Process

The following chapter gives a short introduction to the JURASSIC retrieval processor (Juelich RApid Spectral SIMulation Code), which combines implementations of the fast forward model and a suite of non-linear optimisation methods. It was first conceived as a method for fast trace gas retrievals from Envisat MIPAS measurements (*Hoffmann et al.*, 2005a). JURASSIC was employed to infer trace species from CRISTANF observations (e.g. *Hoffmann et al.*, 2005b; *Weigel et al.*, 2012) and later enhanced to study 2-D retrievals for the PREMIER satellite proposal (e.g. *Ungermann et al.*, 2010a).

## 3.1. Solution of Inverse Problems

Let  $f$  be some physical process, e.g. the process of radiative transfer and measuring infrared light emitted by the atmosphere. The process  $f$  translates the continuous state of the atmosphere  $\tilde{\mathbf{x}}$  into a discrete set of measured radiance values  $\mathbf{y} \in \mathbb{R}^m$ . The measurements  $\mathbf{y}$  are accompanied by normally distributed noise and systematic errors  $\epsilon \in N(0, \sigma)^m$ .

$$\mathbf{y} = f(\tilde{\mathbf{x}}) + \epsilon \tag{3.1.1}$$

An algorithmic approximation of the physical process  $f$  is called a *forward model*  $F \in \mathbb{R}^{(n+n_b) \times m}$ . It calculates measurements from the discretized atmospheric state represented by  $\mathbf{x} \in \mathbb{R}^n$  and  $\mathbf{b} \in \mathbb{R}^{n_b}$ , where  $\mathbf{x}$  contains the quantities to be retrieved and  $\mathbf{b}$  contains all other dependencies.

$$\mathbf{y} = \mathbf{F}(\mathbf{x}, \mathbf{b}) \quad (3.1.2)$$

For brevity,  $\mathbf{b}$  is usually omitted in Eq. 3.1.2, because it remains constant during retrievals.

Reconstructing  $\mathbf{x}$  from the measurements  $\mathbf{y}$  is a process that is historically called “inverting F” or more generally an inverse problem. An inverse problem can only be solved if it is well posed as defined by *Hadamard* (1902), for which three conditions must be met:

- A solution must exist
- The solution must be unique
- The solution must be well behaved. Small changes to the input data must result in small changes to the solution.

In radiative transfer, as in many other cases (e.g. *Engl et al.*, 1996), there is no analytic inverse  $\mathbf{x} = \mathbf{F}^{-1}(\mathbf{y})$ . Unfortunately, inverse problems such as atmospheric remote sensing are commonly ill posed. Due to restrictions on the physical measurement system (e.g. only a finite amount of measurements), there are usually multiple possible solutions, which result in the same simulated spectra. While it is certain that a solution exists, as the measurements are taken from a physical state, even small measurement errors can have a strong influence on the solution.

Transforming Eq. 3.1.2 into a minimisation problem enables us to use many well-studied techniques. The function to be minimised is called cost function and in this case the  $l^2$ -norm of the difference between calculated and real measurements:

$$\min_{\mathbf{x}} \|\mathbf{F}(\mathbf{x}) - \mathbf{y}\|^2 \quad (3.1.3)$$

This basic transformation still has characteristics similar to the direct inverse calculation, but several improvements can be made. By applying pre-whitening (*Rodgers*, 2000, p. 28) through inclusion of a measurement error covariance matrix  $\mathbf{S}_e$ , known correlations between measurements can be removed.

The solution can be made unique and stable by applying a priori knowledge to the problem in the form of a regularisation matrix  $\mathbf{S}_a$  and an a-priori state vector  $\mathbf{x}_a$ . This fixes the solution into a form which

is deemed physically realistic. The construction of this matrix can be varied depending on the problem. For the retrievals of GLORIA data, a Tikhonov regularisation matrix as described by *Tikhonov and Arsenin (1977)* and *Twomey (1977)* or an autoregressive covariance model (*Tarantola, 2004*) is used. The final costfunction  $J(\mathbf{x})$  (*Rodgers, 2000*, p. 84) can be formulated:

$$J(\mathbf{x}) = \|\mathbf{F}(\mathbf{x}) - \mathbf{y}\|_{\mathbf{S}_\epsilon^{-1}} + \|\mathbf{x} - \mathbf{x}_a\|_{\mathbf{S}_a^{-1}} \quad (3.1.4a)$$

$$= (\mathbf{F}(\mathbf{x}) - \mathbf{y})^T \mathbf{S}_\epsilon^{-1} (\mathbf{F}(\mathbf{x}) - \mathbf{y}) + (\mathbf{x} - \mathbf{x}_a)^T \mathbf{S}_a^{-1} (\mathbf{x} - \mathbf{x}_a) \quad (3.1.4b)$$

This cost function tries to minimise the difference between computed and real measurements and simulated and a-priori atmospheric state. The weighting of both terms is determined through the measurement and a-priori covariance matrices.

A non-linear optimisation method can be used to solve  $\min_{\mathbf{x}} J(\mathbf{x})$ . The most prominent method is the Levenberg-Marquardt algorithm (*Marquardt, 1963*), a modification of the Gauss-Newton algorithm. The Newton method finds a root of a function by using the first and second derivatives. The Newton iteration for  $\mathbf{J}'(\mathbf{x}) = 0$ , where  $\mathbf{J}'(\mathbf{x})$  is the first derivative of the cost function, can be formulated as (*Nocedal and Wright, 2006*, p. 254ff.):

$$\mathbf{x}_{i+1} = \mathbf{x}_i + \mathbf{J}''(\mathbf{x})^{-1} (0 - \mathbf{J}'(\mathbf{x})) \quad (3.1.5)$$

Equation 3.1.5 can now be specialised for the cost function  $J(\mathbf{x})$ . Let  $\mathbf{J}'(\mathbf{x})$  and  $\mathbf{J}''(\mathbf{x})$  be the first and second derivative (or the gradient and the Hessian matrix) of the cost function  $J(\mathbf{x})$  (Eq. 3.1.4b):

$$\mathbf{J}'(\mathbf{x}) = 2\mathbf{F}'(\mathbf{x})^T \mathbf{S}_\epsilon^{-1} (\mathbf{F}(\mathbf{x}) - \mathbf{y}) + 2\mathbf{S}_a^{-1} (\mathbf{x} - \mathbf{x}_a) \quad (3.1.6a)$$

$$\mathbf{J}''(\mathbf{x}) = 2\mathbf{F}'(\mathbf{x})^T \mathbf{S}_\epsilon^{-1} \mathbf{F}'(\mathbf{x}) + 2\mathbf{F}''(\mathbf{x}) \mathbf{S}_\epsilon^{-1} (\mathbf{F}(\mathbf{x}) - \mathbf{y}) + 2\mathbf{S}_a^{-1} \quad (3.1.6b)$$

$$\approx 2\mathbf{F}'(\mathbf{x})^T \mathbf{S}_\epsilon^{-1} \mathbf{F}'(\mathbf{x}) + 2\mathbf{S}_a^{-1} \quad (3.1.6c)$$

The Gauss-Newton algorithm is derived from the Newton method by using the approximation shown in Eq. 3.1.6c. For nearly linear prob-

lems, the second derivative of  $F(\mathbf{x})$  is close to zero and it is possible to approximate the Hessian by omitting terms which contain  $F''(\mathbf{x})$ .

$$\begin{aligned} \mathbf{x}_{i+1} \approx \mathbf{x}_i + (\mathbf{F}'(\mathbf{x})^T \mathbf{S}_\epsilon^{-1} \mathbf{F}'(\mathbf{x}) + \mathbf{S}_a^{-1})^{-1} \cdot \\ - (\mathbf{F}'(\mathbf{x})^T \mathbf{S}_\epsilon^{-1} (\mathbf{F}(\mathbf{x}) - \mathbf{y}) + \mathbf{S}_a^{-1} (\mathbf{x} - \mathbf{x}_a)) \end{aligned} \quad (3.1.7a)$$

Calculating the inverse of  $\mathbf{J}''(\mathbf{x})$  in Eq. 3.1.7 is too expensive for all but the smallest problems. Even the matrix-matrix multiplications needed for the calculation of the system matrix should be avoided. Several iterative methods exist for solving a system of linear equations that only require the matrix-vector with the system matrix. The equation  $\mathbf{J}''(\mathbf{x})\mathbf{v} = \mathbf{J}'(\mathbf{x})$  can be solved for  $\mathbf{v}$  by multiplying  $\mathbf{v}$  sequentially by the components of  $\mathbf{J}''(\mathbf{x})$ .

## 3.2. Regularisation

The regularisation matrix  $\mathbf{S}_a^{-1}$  is used to fix the solution to a unique value within the physically possible range. Using the Tikhonov method, the regularisation matrix  $\mathbf{S}_a^{-1}$  can be calculated directly (*Tikhonov and Arsenin, 1977*). The simplest Tikhonov regularisation matrix is the identity matrix, which tries to minimise the distance between  $x$  and  $x_a$ .

The use of difference operators in regularisation was first described by *Twomey (1977)*. A first order difference operator can be used to regularise the shape of the profile. Four matrices  $\mathbf{L}_0, \mathbf{L}_1^x, \mathbf{L}_1^y, \mathbf{L}_1^z$  are used for regularisation of the zeroth and first order and their respective directions,  $\alpha_0, \alpha_1^x, \alpha_1^y, \alpha_1^z$  are scalars that weight the different terms.

$$\mathbf{S}_a^{-1} = \alpha_0 \mathbf{L}_0 + \alpha_1^x \mathbf{L}_1^{xT} \mathbf{L}_1^x + \alpha_1^y \mathbf{L}_1^{yT} \mathbf{L}_1^y + \alpha_1^z \mathbf{L}_1^{zT} \mathbf{L}_1^z \quad (3.2.1)$$

The matrix  $\mathbf{L}_0$  is an identity matrix and is a measure of the difference between  $\mathbf{x}$  and the a priori vector  $\mathbf{x}_a$ . The  $\mathbf{L}_1$  matrices can be constructed by using the single-sided 1-D difference stencil, scaled to the grid size. This method binds the shape of the derived profile to the shape of the a priori profile by penalising large differences in the first derivative of the profiles. For a simple 1-D retrieval with one target and an

equidistant grid with step size  $h$ ,  $\mathbf{L}_1$  can be described as:

$$\mathbf{L}_1 = \frac{1}{h} \begin{pmatrix} -1 & 1 & 0 & \cdots & 0 \\ 0 & -1 & 1 & \cdots & 0 \\ \vdots & \ddots & \ddots & \ddots & 0 \\ 0 & \cdots & 0 & -1 & 1 \\ 0 & \cdots & 0 & 0 & 0 \end{pmatrix} \quad (3.2.2)$$

Each  $\mathbf{L}_1$  matrix can additionally be scaled by the corresponding standard deviations. Then the unit of  $\alpha_1$  is km and roughly corresponds to a correlation length.

In 1-D retrieval, regularisation is applied in the vertical direction. It is, however, possible to use the high horizontal resolution of GLORIA to increase the quality of the retrievals. By applying additional horizontal regularisation it is possible to dampen noise. Regularisation is applied to consecutive 1-D atmospheres scaled by the time between the associated measurements (*Ungermann, 2013*).

## Influence of uncertainties

The measurement error covariance matrix normally only comprises the measurement error. It is also possible to consider other error sources. The full measurement error covariance matrix can be calculated through addition of the various assumed and known contributions to the total error in measurement space:

$$\mathbf{S}_\epsilon = \mathbf{F}'(\mathbf{b}) \cdot \mathbf{S}_b \cdot \mathbf{F}'(\mathbf{b})^T + \mathbf{S}_N \quad (3.2.3)$$

The matrix  $\mathbf{S}_b$  is the covariance matrix for all quantities  $\mathbf{b}$ , which are not retrieved, such as non-target trace gases. It can be transformed into measurement space by multiplying by  $\mathbf{F}'(\mathbf{b})$ , which is the Jacobian matrix of  $F$  with regard to  $\mathbf{b}$ . The matrix  $\mathbf{S}_N$  is the contribution by random noise. In the JURASSIC retrieval scheme, it is assumed that the noise can be divided into two parts. The diagonal matrix  $\epsilon_{\text{Abs}}$  is the covariance matrix of a normally distributed uncorrelated absolute error and the matrix  $\epsilon_{\text{Rel}}$  is additionally scaled by the signal strength.

$$\mathbf{S}_N = \epsilon_{\text{Abs}}^2 + \epsilon_{\text{Rel}}^2 \quad (3.2.4)$$

Using the full measurement error covariance matrix can have severe consequences for the retrieval. Obtaining a real covariance matrix is a difficult endeavour, because most of the correlations between trace gases are either unknown or hard to quantify correctly. We use profiles and variances from the climatology by *Remedios et al.* (2007). While important trace gases have well-known distributions, most of the faint emitters (e.g. CFC-113, SF<sub>6</sub>) have to be regarded with care. Using a measurement error covariance matrix derived from this dataset in the retrieval does not introduce any biases in the climatology into the retrieval. Especially absolute values may have a large uncertainty.

In the regularisation matrix this can be dealt with easily: By using a first order regularisation, we regularise profiles shapes instead of absolute values, which predetermines the results to a much smaller extent. The measurement error covariance matrix weights different integrated spectral windows according to their associated errors. Windows with higher errors have less influence on the retrieval result. However, the real covariance matrix  $\mathbf{S}_b$  is usually unknown. Unfortunately, approximations from an autoregressive model (*Tarantola*, 2004) can impose a bias on the retrieval.

Instead, a diagonal matrix  $\mathbf{S}_{\text{quick}}$  is used that only contains influences from noise and an approximation  $\epsilon_{\text{FM}}$  of the general forward model errors. This is especially important in the 3-D tomographic retrievals, because it would not be feasible to calculate and store a full matrix. The full measurement error covariance matrix can only be calculated if the Jacobian matrix with respect to  $b$  is known.

$$\mathbf{S}_{\text{quick}} = \mathbf{S}_N + \text{diag}(\epsilon_{\text{FM}} * \mathbf{y}) \quad (3.2.5)$$

### 3.3. Forward Model

The radiative transfer equation describes how light is emitted, absorbed and re-emitted in the atmosphere. For infrared radiation in the atmosphere, it is given by:

$$I(\nu) = \int_0^\infty B(\nu, T(s)) \frac{d\tau(\nu, s)}{ds} ds \quad (3.3.1)$$

The spectral radiance  $I$  at wavelength  $\nu$  is the integral of all light

transmitted along the line of sight starting from the detector at  $s = 0$  (see Figure 2.1). The Planck function  $B$  for the temperature  $T$  of the atmosphere at  $s$  and the spectroscopic constants  $c_1$  and  $c_2$  can be calculated by:

$$B(\nu, T(s)) = \frac{c_1 \nu^3}{e^{c_2 \nu / T} - 1} \quad (3.3.2)$$

In the case of thermal infrared radiation, scattering can be omitted in clear sky scenarios as the wavelengths involved are too long to be efficiently scattered by air molecules. The source term from deep space can be omitted, too.

Assuming local thermodynamic equilibrium, the transmissivity  $\tau$  can be calculated from the contribution of spectral lines of trace gas emitters and the aerosol extinction coefficient  $\sigma_e$ . Important parameters for each line are the line strength  $k$ , the line shape  $f$ , which depends on pressure  $p$  and temperature  $T$ , and the density  $\rho$ .

$$\tau(\nu, s) = \exp \left( - \int_0^s \sigma_e(\nu, x) dx - \sum_i \sum_j \int_0^s k_{ij}(T(x)) f_{ij}(\nu, p(x), T(x)) \rho_i(x) dx \right) \quad (3.3.3)$$

To simulate a measurement, the instrument line shape  $w_{\text{ILS}}$  and the field of view  $w_{\text{FOV}}$  have to be considered. The instrument line shape (ILS) is a consequence of the finite spectral resolution of an instrument. For a Fourier transform spectrometer, the ILS is normally a sinc function, but can be modified by apodization to a function which drops to zero faster. This is done with the Norton-Beer apodization function (Norton and Beer, 1976) in the case of GLORIA.

The field of view function is defined over a sphere with azimuth  $\phi \in [0, 2\pi]$  and elevation  $\theta \in [-\frac{\pi}{2}, \frac{\pi}{2}]$ . Taking the ILS and the FOV into consideration, the radiance value of one spectral sample  $I^k$  is:

$$I^k = \int_0^{2\pi} \int_{-\frac{\pi}{2}}^{\frac{\pi}{2}} w_{\text{FOV}}(\phi, \theta) \int_0^\infty w_{\text{ILS}}(\nu) I(\nu) d\nu d\theta d\phi \quad (3.3.4)$$

To obtain high accuracy spectra,  $I(\nu)$  is often calculated in a line by line fashion with a very fine spectral sampling, which is computationally very expensive. As a faster alternative, the JURASSIC forward model is based on the emissivity growth approximation. EGA is an approximate radiative transfer calculation scheme that can use spectrally averaged or integrated, tabulated emissivity values. The JURASSIC forward model uses tabulated emissivity values for all emitter, temperature, pressure, and number density combinations (*Gordley and Russell III, 1981*) encountered. It is sufficient to calculate emissivity values for the instrument’s spectral grid, which already include the spectral integration over the ILS (*Riese et al., 1997*).

$$\hat{\epsilon}(\nu) = \int_0^\infty w_{\text{ILS}} \epsilon(\nu) \quad (3.3.5)$$

The underlying monochromatic emissivities are calculated for homogeneous gas cells by accounting for the full-line physics. Compared to line-by-line calculations, a speedup of three orders of magnitude or more can be achieved.

Emissivities for a specific state of the atmosphere are calculated by linear interpolation in the pre-calculated values. The tables are adaptively refined in number density during creation until a sufficiently small interpolation error is achieved. The calculation of emissivity from optical paths includes an exponential function, which is notoriously difficult to approximate with a linear interpolation. As an optimisation the values are stored as optical paths, which reduces the number of points needed to achieve an interpolation error bound. A first principles derivation of the algorithm used to calculate table entries is included in Appendix C.

JURASSIC is not only capable of simulating GLORIA in its different modes, but also supports CRISTA-NF, a height scanning instrument, and a planned 2-D tomographic satellite instrument. The radiative transfer is usually calculated along infinitesimally thin lines called pencil beams. How these pencil beams are combined with the field of view to form the measurements is described in an instrument model. The basic building block of “the detector” is called “superpixel” and represents one sensitive element. Multiple spectral ranges may be assigned to each superpixel to form a measurement or “observation”. To simulate the field of view of each superpixel, one or more pencilbeams are calculated and combined

via a weighting matrix. One pencilbeam can have influence on multiple superpixels. This is especially useful in imaging detectors like GLORIA, where the FOV from multiple superpixels overlaps significantly.

## 3.4. Retrieval Technique

Two different atmospheric representations were used for this work. For easier grid generation, atmospheric layers are considered to be plane-parallel. Variations of temperature, pressure and trace gases in the horizontal are much lower compared to variations in the vertical. It is thus a good approximation to assume horizontal homogeneity. With this assumption, it is possible to use a single height scan to retrieve various atmospheric quantities. For 3-D tomographic retrievals, we use a full 3-D representation of the atmosphere to retrieve important 3-D structures (see Chapter 7.2).

For the particularly demanding task of 3-D retrievals, new methods had to be implemented. In order to manage the increasing complexity, the original code was partly rewritten in Python and C++, which now forms the core of JURASSIC2. To accommodate the 3-D retrieval technique, the instrument model was improved to allow more instrument configurations. The control code uses Python as a primary language to facilitate a rapid development cycle. Performance-critical code is implemented in C++. To calculate the Jacobian matrices, a new adjoint model (*Lotz et al.*, 2011) was added.

## 3.5. 3-D Tomographic Retrievals

Atmospheric exchange processes, which are most interesting for scientific studies, are closely linked to small-scale 3-D structures. In this case, the key assumption of 1-D retrievals no longer holds true: The atmosphere can not be simulated as horizontally homogeneous. Across the line of sight, the resolution is given by the field of view and the measurement time in conjunction with the speed of the aircraft, which is about 10 km for GLORIA and is in a range which allows the observation of small-scale structures. In contrast, the resolution along the line of sight for a single measurement is about 200 km as a result of the weighting function of

the radiative transfer. This is coarse compared to important mesoscale processes of the UTLS. Variations of temperature and trace gases are smoothed out along this direction, which may lead to significant biases in the retrieval results.

A technique similar to computed tomography can be used to reconstruct a 3-D volume, if measurements from many directions are available. In CT Scanners, a direct reconstruction based on the Radon transform (*Radon, 1917*) can be applied. This cannot be done with measurements from GLORIA because the geometry is too complex. The Radon transform can only be used when all measurements are within one plane. Additionally, direct methods have difficulty handling missing angles in the measurement data, which will always occur in measurements from aircraft-based instruments. In most cases GLORIA is on a linear flight path, which limits the range of viewing angles to  $90^\circ$  (from  $45^\circ$  to  $135^\circ$  w.r.t. the flight direction) that can be acquired with instrument panning (*Ungermann et al., 2011*). Even when a closed loop flight pattern is used (*Ungermann et al., 2010b*), there are missing measurements when the aircraft turns. Due to restrictions in flight planning, polygonal patterns are used to approximate circles.

## 4. Automatic Spectral Window Selection

The selection of spectral information used by the retrieval algorithms is essential for the quality of retrieval results. Different wavelength regions contain emissions from different trace gases, have different noise characteristics and different systematic errors. This selection is usually made by informed decision, based on experience from previous experiments and trial and error testing. With the reduced spectral resolution of the dynamics mode, spectral lines are no longer distinguishable in the spectrum. Each sample contains contributions from multiple trace gases, sometimes in similar proportions. The high number of different contributions makes it much more difficult to estimate the quality of a spectral sample. A more objective method is therefore needed to choose a selection of microwindows.

This chapter provides a method of selecting spectral windows based on a measure of the information gain by a retrieval. A spectral window or microwindow is a small selection of adjacent spectral samples. If only the average of a microwindow is used in the retrieval, it is called an integrated spectral window. Retrievals generally use multiple integrated spectral windows in JURASSIC. Because the selection of microwindows is done a priori, an atmospheric state is used that is representative of the expected conditions.

Let  $\hat{\mathbf{x}}$  be an approximation of the mean value of the physically realistic atmospheric states, derived from climatological information. If we assume that all errors are normally distributed, we can calculate the gain matrix  $\mathbf{G} \in \mathbb{R}^{n \times m}$ , which maps changes in the radiance measurements to changes in retrieved atmospheric quantities.

$$\mathbf{G} = (\mathbf{S}_a^{-1} + \mathbf{F}'(\hat{\mathbf{x}})^T \mathbf{S}_\epsilon^{-1} \mathbf{F}'(\hat{\mathbf{x}}))^{-1} \mathbf{F}'(\hat{\mathbf{x}})^T \mathbf{S}_\epsilon^{-1} \quad (4.0.1)$$

The product of  $\mathbf{G}$  and the Jacobian matrix  $\mathbf{F}'(\hat{\mathbf{x}})$  is called the averaging kernel and can be used to calculate the retrieval error covariance matrix  $\mathbf{S}_x$ . The averaging kernel describes the smoothing influence of the regularisation and the finite resolution of the instrument. It describes the way the retrieval transforms the *true* state into the retrieval result.

$$\mathbf{S}_x = (\mathbf{I} - \mathbf{G}\mathbf{F}'(\hat{\mathbf{x}})) \mathbf{S}_a \quad (4.0.2)$$

This lets us compute the quantity  $E_{\mathbf{S}_x}$ , which is the entropy of  $\mathbf{S}_x$  in bits. It is a figure of merit for the information value and represents our knowledge of the atmospheric state (*Shannon, 1948*).

$$E_{\mathbf{S}_x} = -\frac{1}{2} \log_2(\det(\mathbf{S}_x)) \quad (4.0.3)$$

The change in entropy  $H$  from before the retrieval as described by the a priori covariance matrix  $\mathbf{S}_a$  to the retrieval error covariance matrix  $\mathbf{S}_x$ , which includes the knowledge from measurements, is called information gain (*Kullback and Leibler, 1951*):

$$H = E_{\mathbf{S}_x} - E_{\mathbf{S}_a} = -\frac{1}{2} \log_2 \left( \frac{\det(\mathbf{S}_x)}{\det(\mathbf{S}_a)} \right) = -\frac{1}{2} \log_2(\det(\mathbf{I} - \mathbf{G}\mathbf{F}'(\hat{\mathbf{x}}))) \quad (4.0.4)$$

A selection of microwindows can now be rated by their information gain  $H$ . Microwindows with higher information gain provide a greater increase in our knowledge about the atmosphere by decreasing the uncertainty after the retrieval. An optimal selection would have the maximal increase in entropy possible for a given set of initial conditions.

The determinant is typically calculated by performing an LU decomposition (*Householder, 1975*) of the  $n \times n$  matrix, which can be quite expensive, but includes further valuable information. Consider a retrieval setup with two targets and two spectral windows. The primary target emits in the first window, the second target emits in the second window, but has some minor spectral lines in the other spectral range. Improving our knowledge of the second target also decreases the uncertainty of the primary target. This influence is represented by off-axis elements in  $\mathbf{S}_x$ .

In our retrieval scheme, microwindows containing radiation from more than one emitter is the common case.

## 4.1. Advanced Information Content

If the approximate measurement covariance matrix  $\mathbf{S}_{\text{quick}}$  (see Eq. 3.2.5) is used in the retrieval, the definition of the gain matrix does not contain the proper covariances for calculating the information content. Using the definition of  $\mathbf{S}_x$  in 4.0.2 limits the errors considered in the information content to errors included in our retrieval, while we want to know the information gain compared to a full measurement covariance matrix.

We can change the definition of  $\mathbf{S}_x$  to Eq. 4.1.1, which splits the matrix into the measurement error  $\mathbf{S}_m$ , the smoothing error  $\mathbf{S}_s$  and systematic errors by uncertainties in other trace gases  $\mathbf{S}_f$ :

$$\mathbf{S}_x = \mathbf{S}_m + \mathbf{S}_s + \mathbf{S}_f \quad (4.1.1)$$

The individual error matrices can be expressed as follows:

$$\mathbf{S}_m = \mathbf{G} \cdot (\mathbf{S}_N + \mathbf{S}_{\text{Shift}}) \cdot \mathbf{G}^T \quad (4.1.2a)$$

$$\mathbf{S}_s = (\mathbf{F}'(\hat{\mathbf{x}})^T \mathbf{S}_q^{-1} \mathbf{F}'(\hat{\mathbf{x}}) + \mathbf{S}_a^{-1}) \cdot \mathbf{S}_a^{-1} \cdot (\mathbf{F}'(\hat{\mathbf{x}})^T \mathbf{S}_q^{-1} \mathbf{F}'(\hat{\mathbf{x}}) + \mathbf{S}_a^{-1}) \quad (4.1.2b)$$

$$\mathbf{S}_f = \mathbf{G} \cdot \mathbf{S}_\epsilon \cdot \mathbf{G}^T \quad (4.1.2c)$$

In this representation, the matrix  $\mathbf{S}_f$  includes the influence of the full covariance matrix.

## 4.2. Evaluating Selections

The automatic selection based on maximising the information gain may generate apparently surprising choices when compared to hand-picked ensembles, where microwindows are normally selected on the basis of known strong signatures from trace gases.

For analysis purposes, it would be helpful to have a measure of the information gain of traces gases provided by a specific microwindow. With the definition of information content from Eq. 4.0.4, we know that

the influence of the retrieval on a target is defined by the determinant of the matrix  $\mathbf{I} - \mathbf{GF}'(\hat{\mathbf{x}})$ . We assume that all other quantities are known to their a priori standard deviations and select a sub-matrix defined by the lines and columns associated with the trace gases to be retrieved.

Let  $Q_1$  to  $Q_3$  be quantities of interest:

$$\mathbf{M} = (\mathbf{I} - \mathbf{GF}'(\hat{\mathbf{x}})) = \begin{matrix} & \begin{matrix} Q_1 & Q_2 & Q_3 \end{matrix} \\ \begin{matrix} Q_1 \\ Q_2 \\ Q_3 \end{matrix} & \begin{pmatrix} \mathbf{M}_{11} & \mathbf{M}_{12} & \mathbf{M}_{13} \\ \mathbf{M}_{21} & \mathbf{M}_{22} & \mathbf{M}_{23} \\ \mathbf{M}_{31} & \mathbf{M}_{32} & \mathbf{M}_{33} \end{pmatrix} \end{matrix} \quad (4.2.1)$$

We can now calculate their isolated information contents:

$$H_1 = -\frac{1}{2} \log_2(\det(\mathbf{M}_{11})) \quad (4.2.2a)$$

$$H_2 = -\frac{1}{2} \log_2(\det(\mathbf{M}_{22})) \quad (4.2.2b)$$

$$H_3 = -\frac{1}{2} \log_2(\det(\mathbf{M}_{33})) \quad (4.2.2c)$$

The number of microwindows in the calculation of  $\mathbf{M}$  can be varied to gain additional information. If we include all microwindows, we obtain information about the whole ensemble. A single microwindow is analysed by removing it from the ensemble and recalculating the information gain. The difference to the results from the full ensemble is the information gain from this microwindow.

## Aerosol-like extinction coefficients

In our retrieval scheme, we use an aerosol-like extinction coefficient as an approximation of real aerosols, instrument effects and unknown trace gases. In our trace gas retrievals, the aerosol is only a secondary target. Adding a correct aerosol model would increase the complexity considerably. Additionally, a priori information, such as the type of aerosol encountered, would be needed. We can, however, assume that the influence of aerosol on spectral radiance through grey body emission and scattering changes much more slowly with wavelength than light emitted by molecular gases. The aerosol scheme typically employed in JURAS-SIC assumes that the influence of aerosols is not wavelength-dependent,

as we do not have the necessary data to implement realistic aerosol profiles.

As a minor target, we would like to have the ensemble not specifically optimised for aerosol retrievals. Instead microwindows for aerosol should still be chosen, if they improve the result for other targets. Equation 4.2.1 yields a simple way to exclude a single target from optimisation. We remove lines and columns associated with aerosol extinction coefficients from  $\mathbf{I} - \mathbf{GF}'(\hat{\mathbf{x}})$ . Influences on other trace gases are still included via the matrix multiplication leading to Eq. 4.1.1.

Let  $Q_2$  be the state vector of an aerosol extinction coefficient, then the new information content is  $H^*$ :

$$\mathbf{M}^* = \begin{matrix} & Q_1 & Q_3 \\ Q_1 & \begin{pmatrix} \mathbf{M}_{11} & \mathbf{M}_{13} \\ \mathbf{M}_{31} & \mathbf{M}_{33} \end{pmatrix} \\ Q_3 & \end{matrix} \quad (4.2.3)$$

$$H^* = -\frac{1}{2} \log_2(\det(\mathbf{M}^*)) \quad (4.2.4)$$

Our forward model can associate different height-dependent aerosol extinction coefficients with different microwindows. Three different configurations were tested: one extinction coefficient for the whole spectral range from 780 to 1400  $\text{cm}^{-1}$  assuming no spectral dependency, changing the extinction coefficient every 60  $\text{cm}^{-1}$  to accommodate a strong spectral dependency, and using a small number of hand-picked intervals.

Retrieval done with the ESSenCe dataset shows that having only one extinction coefficient does not accommodate the natural variability well enough. Our initial estimate of sufficiently constant behaviour within 60  $\text{cm}^{-1}$ , however, proved to be too conservative. Adjacent aerosol ranges yielded strongly correlated profiles. By merging them, it is possible to use fewer and broader aerosol ranges. In this way it can be ensured that distinct spectral features, such as the  $\text{HNO}_3$  signature at 890  $\text{cm}^{-1}$ , are contained within one aerosol range to avoid inconsistencies.

## Genetic algorithm

In dynamics mode, it is not usually possible to separate spectral lines for a species. The radiation measured in a microwindow is a sum of contributions from several different species. To recover an accurate trace gas

distribution, all targets must be evaluated in a simultaneous retrieval. The selection of microwindows should provide the maximal information content considering all retrieved and interfering species. Testing every possible combination quickly becomes computationally unfeasible, especially if the size of the microwindows may vary. A dynamics mode GLO-RIA measurement contains  $\approx 1000$  spectral samples. A full evaluation of all microwindow sets with 5 samples would require  $10^{15}$  evaluations. Previous methods work by growing microwindows (successively adding spectral samples) within a pre-selected broader spectral range. The broader spectral range is either hand-picked (*von Clarmann and Echle, 1998*) or based on optimising only one microwindow at a time (*Dudhia et al., 2002*).

It is possible to weaken one of the requirements for the optimisation method, so that it is sufficient to find a solution that is close to the optimum. The algorithms involved in calculating the information gain are not an exact replication of the physical process and the information on trace gases, which is taken from a climatology is not perfect either. This makes it possible to use stochastic methods like a genetic algorithm (GA).

A genetic algorithm is an optimisation method suitable in situations in which the problem representation is not numerical (e.g. a selection of items, a set) and no derivatives exist (*Mitchell, 1998*). A GA is modelled on the natural evolution of species. One microwindow is encoded as the window position and window size which is equivalent to a gene. A genome consists of a vector of these pairs. The length of the genome defines the number of microwindows. One iteration in this algorithm is usually called a generation. The first generation is initialised by randomly generated individuals. From these parents a new generation is generated by crossover and mutation. Crossover randomly recombines the genome of two parent individuals and is an abstraction of sexual reproduction in biology. It is implemented by designating a cut index and swapping the genome of the parents (Figure 4.1). Additionally, mutations refresh the available gene pool by randomly changing single genes. Algorithm 1 shows a pseudo-code implementation of a genetic algorithm.

We use the information content described in Section 4.2 as a figure of merit for the fitness of an individual. After all individuals are evaluated, we select the best ones as the parents for the next generation in our algorithm.

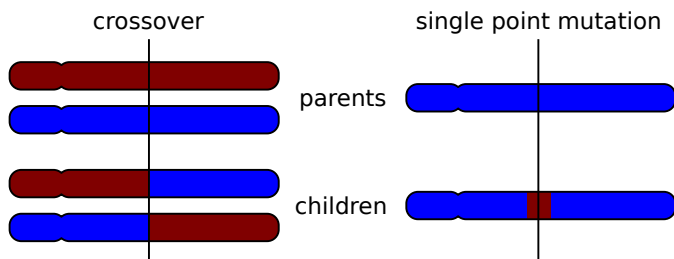


**Figure 4.1:** Examples of crossover and mutation as used in the genetic algorithm

It is possible to use a variety of stopping criteria. Common choices are the number of generations or an absolute value for the fitness, if the maximum value is known.

---

#### **Algorithm 1** Genetic Algorithm

---

Generate Parents

**while** Running **do**

    Produce New Generation

    Evaluate Fitness

    Select Best Individuals as New Parents

**end while**

---

## 4.3. Implementation

A method is needed to calculate the information gain of a selection as fast as possible. The fast forward model and the kernel algorithms provided by JURASSIC can be used to pre-calculate the kernel matrices. Assuming a spectral range from 780 to 1400  $\text{cm}^{-1}$  with a spectral sampling of 0.625  $\text{cm}^{-1}$ , there are only  $\approx 10^3$  spectral samples to calculate. Microwindows with a width larger than one spectral sample are calculated by adding the appropriate Jacobian matrices, similar to the physical process. The regularisation matrix  $\mathbf{S}_a$  and the covariance matrix  $\mathbf{S}_e$  are also generated during the preprocessing. When running the genetic algorithm, only a series of matrix operations is needed to calculate the information gain.

The genetic algorithm can be run efficiently in parallel, as only the rather small genomes need to be exchanged between the processes before and after evaluation of a new generation. The defining part of the work is calculating the fitness of each genome by using the information gain method. Overall, the runtime is dominated by matrix multiplication and inversion and accordingly scales with  $O(n^3)$  in the number of microwindows.

#### 4.4. Spectral Window Selection for the GLORIA Instrument

A priori data for the selection process is taken from Remedios MIPAS reference atmospheres (*Remedios et al.*, 2007). This includes profiles for trace gases, temperature and pressure, and their variances.

We expect a radiometric offset, which is normally distributed and can be decreased by combining several spectral samples (noise-equivalent spectral radiation, NESR). According to the technical specifications, the noise will not depend upon signal strength. To accommodate yet unknown or unquantified effects, e.g. inaccuracies in the calibration, we simulated a 0.1% gain, which is not reduced by broader microwindows.

A setup with multiple targets was created for the evaluation of the ESSenCe data. Temperature,  $\text{HNO}_3$ ,  $\text{O}_3$ , and CFC-11 were included as primary targets and CFC-12, peroxyacyl nitrate (PAN), and  $\text{ClONO}_2$  were included as secondary targets. Several other emitters were included to account for their contributions as interfering trace gases. In total, 13 different quantities were derived as specified in Table 4.1, while simulating 20 trace gases, temperature, and pressure. The search was restricted to samples below  $1000 \text{ cm}^{-1}$ , as  $\text{CH}_4$  was not included as a target.

Primary	Temperature, $\text{HNO}_3$ , $\text{O}_3$ , CFC-11
Secondary	CFC-12, PAN, $\text{ClONO}_2$
Tertiary	Offset, $\text{CCl}_4$ , $\text{H}_2\text{O}$ , Aerosol 1-3

**Table 4.1:** Retrieval targets

Multiple optimization runs were executed with different numbers of microwindows. Each generation consisted of 1000 individuals, from which

30 were selected as the parents of the next generation.

In the end, 12 microwindows were included in the setup, which matches number of integrated spectral windows to the number of full profile targets, leading to an approximate equality in the number of information-carrying values provided and the number of unknowns in the retrieval. Figure 4.2 shows the value of the fitness function of multiple independent runs of the optimisation algorithm over the course of 500 generations. To assume convergence all the final fitness values of all runs should be within 10% of each other. If this is not the case, the number of generations and the generation size should be increased to improve convergence.

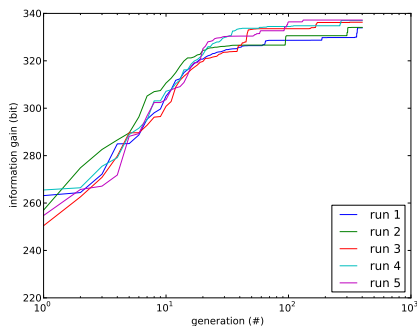


**Figure 4.2:** Representative evolution of the fitness function after successful genetic optimisation

The results of the best run were selected as retrieval setup. Figure 4.3 shows the microwindows of this retrieval setup, as well as selected primary and secondary emitters. The method described in Section 4.2 can now be used to analyse the setup. Table 4.2 shows the two top contributions for each microwindow. The primary reason why each microwindow was chosen can also be deduced from an informed look at the spectra in Figure 4.3, however an objective value is now connected to each microwindow. The algorithm selected the CO<sub>2</sub> Q-Branch at 792 cm<sup>-1</sup>, which can be used to retrieve temperature profiles (e.g. *Riese et al.*, 1997, 1999). Our analysis confirms this and sets the information gain for temperature at the first position to 28.0 bit. Similar behaviour can be observed when looking at other major trace gases, such as HNO<sub>3</sub> and CFC-11.

Although the information content of aerosol had no direct influence during the optimisation, one spectral window can be attributed to each aerosol profile.

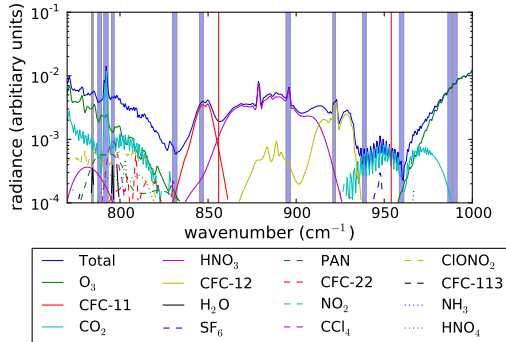


**Figure 4.3:** Spectral band between  $770 \text{ cm}^{-1}$  and  $1000 \text{ cm}^{-1}$ , showing the selected microwindows for the full retrieval setup

Microwindow $\text{cm}^{-1}$	primary	bit	secondary	bit
784.0625 - 784.6875	H <sub>2</sub> O	22.0	CCl <sub>4</sub>	4.6
787.5000 - 789.3750	PAN	18.8	H <sub>2</sub> O	8.4
790.9375 - 793.1250	temperature	28.0	O <sub>3</sub>	19.8
795.3125 - 796.5625	CCl <sub>4</sub>	14.4	H <sub>2</sub> O	1.6
830.0000 - 832.1875	aerosol	33.5	F11	14.9
845.3125 - 847.1875	CFC-11	28.8	temperature	2.5
894.3750 - 896.5625	HNO <sub>3</sub>	71.4	CFC-12	4.3
920.9375 - 922.1875	CFC-12	26.2	temperature	2.5
937.8125 - 939.6875	aerosol	62.6	HNO <sub>3</sub>	44.2
958.7500 - 960.9375	aerosol	86.7	O <sub>3</sub>	35.4
986.2500 - 988.1250	O <sub>3</sub>	5.4	PAN	0.5
989.0625 - 991.2500	O <sub>3</sub>	6.7	PAN	0.7

**Table 4.2:** Selected microwindows and primary and secondary associated targets by information gain

## 5. ESSenCe Campaign

The ESA Sounder Campaign (ESSenCe) provided the first opportunity to operate GLORIA on an aircraft. The campaign was conducted with the Russian M-55 Geophysica high altitude research aircraft (Figure 5.1). The Geophysica has an operational ceiling of 21 km, which allows measurements at altitudes that are inaccessible to other aircraft. ESSenCe was planned to include two technical and two scientific flights from Kiruna, Sweden, during December 2011. Due to technical difficulties only the first two flights could be performed. Primary objectives were testing the GLORIA instrument under flight conditions and the study of processes influencing the composition of the UTLS.



**Figure 5.1:** The Russian M-55 Geophysica high altitude research aircraft during integration of the scientific instruments for ESSenCe. GLORIA is mounted in the front bay.

GLORIA was mounted in the front bay of the Geophysica. The second

bay was occupied by the MARSCHALS instrument. MARSCHALS is a millimetre wave limb sounder, which complements GLORIA with its ability to take measurements in the presence of high clouds. The MIPAS-STR instrument was mounted in its dome on top of the aircraft. Several in situ instruments were also included in the payload. Some of these instruments were used to validate the GLORIA results.

(a) Flight path of flight 1 on 11th December 2011      (b) Flight path of flight 2 on 16th December 2011

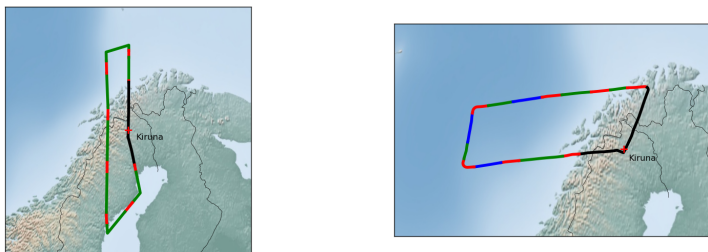


**Figure 5.2:** Flight paths of the ESSenCe campaign. Planned measurement modes: park position, instrument locked (black); calibration, measuring black bodies (red); chemistry mode, high spectral resolution (green), dynamics mode, high temporal resolution (blue)

## 5.1. GLORIA Data Processing

The processing of GLORIA data consists of several steps. Raw measurements come directly from the analog digital converter and are stored in dimensionless detector counts. These have to be converted to proper spectra during the level 1 data processing based on calibration results. The calibration is mostly based on the method of *Brault* (1996). Raw interferograms are a series of measurements equally spaced in time. They must be resampled into position space with a velocity signal generated by a reference laser. The interferogram is then converted into frequency space by a Fourier transformation.

A black body measurement with a known temperature and emission

is used to calculate the gain of each detector pixel. Due to the relatively warm spectrometer body, there is a significant background (base line) in the spectrum. The base line represents non-atmospheric emission that can be removed by two different approaches. The first approach uses two black body measurements at different temperatures to extrapolate a 0 K black body that only contains base line emissions. An alternative is to use an upward looking deep space measurement with little or no atmospheric emission as the baseline (*Höpfner et al.*, 2000). From the black body measurements, a gain and an offset value is derived for each pixel. This calibration data is applied to all atmospheric measurements. The measurements are spectrally calibrated by scaling the spectra in wavenumbers to match selected CO<sub>2</sub> lines with known line positions. The detector was read out with 128 rows and 48 columns. The radiance is averaged over columns to increase the signal-to-noise ratio.

One major change in the design of the interferometer from MIPAS-STR to GLORIA was the change from driving the movable arm(s) with a double pendulum to a linear drive. This was expected to remove the influence of vibration on the interferogram. The fixed corner cube was, however, excited by vibrations from the aircraft, which led to a large apparent velocity jitter during both flights. During the first flight, vibrations were intense enough to move the sled effectively backwards, which could not be corrected by the post flight processing. For the second flight, the speed of the linear drive was increased, which allowed the data to be used.

The two black bodies proved to be difficult to cool to their designated temperatures due to the low air pressure at flight altitude. A tentative calibration from two black bodies contained significant artefacts, which prohibited successful trace gas retrievals. Instead a calibration between deep space measurements and one black body was chosen. The resulting spectra were free from obvious artefacts, apart from certain spectral ranges with strong emission lines present even in deep space geometry. These were, most importantly, the 10  $\mu\text{m}$  ozone band and a methane band at 8  $\mu\text{m}$ . In these ranges, the instrument self-emissions, which were derived from the deep space measurements, were overestimated, which led to an underestimation in the calibrated spectra. The spectral sampling is 0.3125  $\text{cm}^{-1}$  and the spectral resolution is  $\approx 0.6 \text{ cm}^{-1}$  after apodization.

## Cloud filtering

For the retrieval of trace gases from infrared limb measurements, clear sky spectra are preferred. Infrared radiation is not scattered by air molecules and therefore no computationally expensive scattering code is needed (see 3.3). Cloud identification is done by computing one of the MIPAS cloud indices (*Spang et al.*, 2004), which compares incident radiation from two different spectral ranges. While multiples of these colour indices are defined, the ratio between mean radiances of  $788.20\text{--}796.25\text{ cm}^{-1}$  and  $832.30\text{--}834.40\text{ cm}^{-1}$  is used, because of the large contrast between the  $\text{CO}_2$  Q-Branch and the background.

Figure 5.3 shows the cloud index calculated from GLORIA measurements. Values are very low for most observations during the whole measurement period. A cloud index larger than 4 is normally considered to be a clear sky. Comparing a cross section of the GLORIA cloud index to data from MIPAS-STR shows good agreement: MIPAS-STR measured very low cloud indices over the whole flight (Figure 5.4).

## Aerosol

The MIPAS Envisat instrument was still operating during the ESSenCe campaign. Figure 5.5 shows cloud information from orbit 51228, measured on 16th December 2011, derived from processing different colour indices. Especially north of the flightpath, there was a high level of background aerosols and polar stratospheric clouds (PSCs) at flight level and above. PSCs are stratospheric clouds which form only at very low temperatures ( $< 195\text{ K}$ ). This may also have a negative influence on the calibration by introducing a high bias with a spectral dependency into the deep space measurements, which could have degraded the quality of the calibration. The lower altitudes were contaminated with aerosol from the Nabro eruption up to a maximal altitude of 14 km. The Nabro volcano is situated in Eritrea near the Red Sea. It is marked with a red triangle in Figure 5.6. The eruption on 13 June 2011 injected  $\text{SO}_2$  directly into the stratosphere and more was later uplifted by the Asian monsoon (*Sawamura et al.*, 2012). The  $\text{SO}_2$  was transported north and formed an extended aerosol layer over the whole arctic region during winter 2011 (*von Hobe et al.*, 2013).

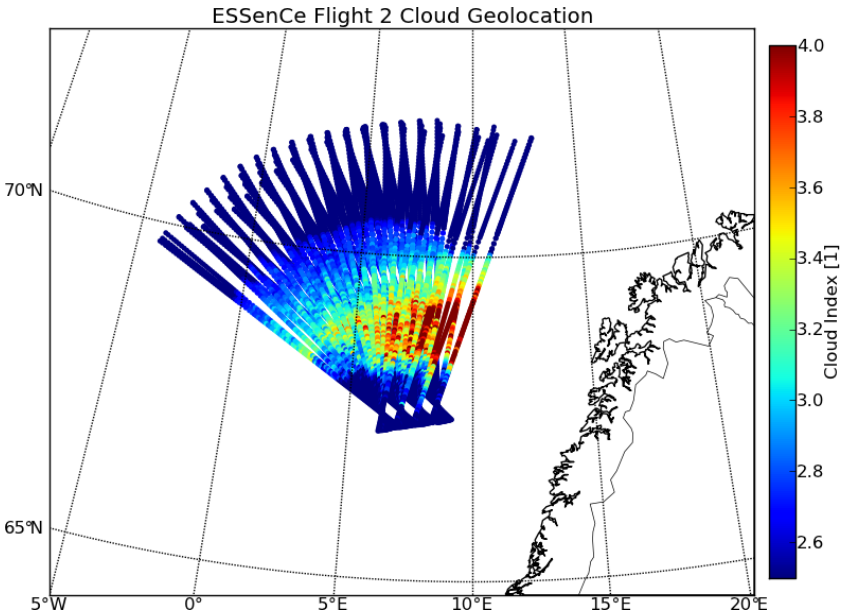


**Figure 5.3:** Cloud indices from GLORIA measurements at tangent point locations. Values smaller than 4 are indicative of clouds in the line of sight. Figure by courtesy of Tobias Guggenmoser.

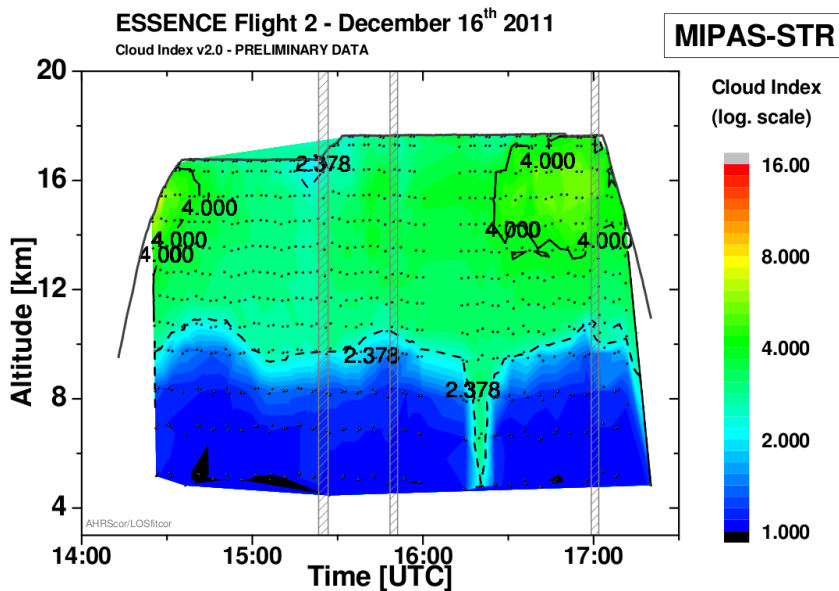


**Figure 5.4:** Cross section with cloud indices from MIPAS-STR. Higher values indicate clear sky conditions. Figure by courtesy of Wolfgang Woivode.

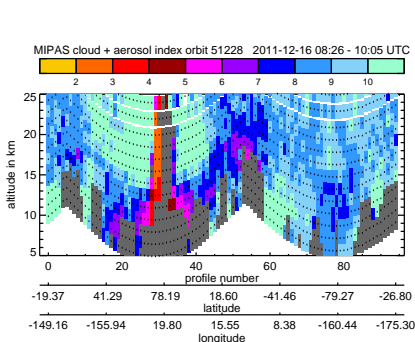


**Figure 5.5:** Cloud detection from MIPAS Envisat. Ice clouds are filtered. Area of ESSenCe measurements is at column 35. Figure by courtesy of Sabine Griebbach.

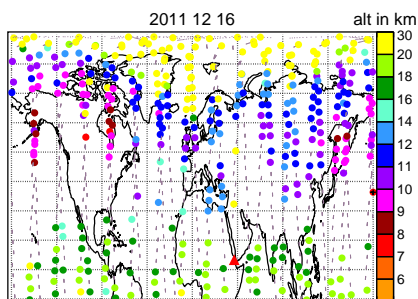


**Figure 5.6:** Cloud top altitude from MIPAS Envisat. Ice clouds are filtered. The Arctic is covered by high STS or PSCs, at the border of the vortex the SO<sub>2</sub> aerosol layer can be seen at 14 km. Figure by courtesy of Sabine Griebbach.

## 5.2. Error Estimates, A Priori and Model Data

In the measurement error covariance matrix used for retrievals no influences of background trace gases are included. Instead, a fast approximation is used consisting only of the noise and a forward model error relative to the total radiance is used. The size of the forward model error due to this approximation is determined by comparing the JURASSIC forward model to the Reference Forward Model (RFM, see *Dudhia, 2000; Ungermann et al., 2012b*).

A priori data is taken from the Remedios MIPAS reference atmospheres (*Remedios et al., 2007*). To account for the increase in the concentration of CO<sub>2</sub> since the creation of the climatology, the surface values were corrected with recent measurements from Mauna Loa, while keeping the height gradient intact.

For PAN a zero profile is used a priori, because the MIPAS reference atmospheres do not contain values for this trace gas. The standard deviation for PAN was assumed to be in the range of the absolute values observed in a WACCM4 model run (*Garcia et al., 2007*). The error analysis in Section 5.3 shows no significant contribution of PAN to the overall error. Values for pressure and temperature were taken from the ECMWF ERA-Interim dataset (*Dee et al., 2011*).

Source	Products used
MIPAS reference atmospheres	default
CLaMS	ClONO <sub>2</sub>
WACCM4	PAN
ECMWF ERA-Interim	pressure, temperature

**Table 5.1:** A priori data used for the retrievals

A pointing correction of 0.1955° was derived by using an elevation angle retrieval to fit the limb radiance data from GLORIA in the spectral region of the CO<sub>2</sub> Q-Branch at 792.5 cm<sup>-1</sup> to limb radiance values corresponding to ECMWF temperature profiles.. This offset was used for all retrievals.

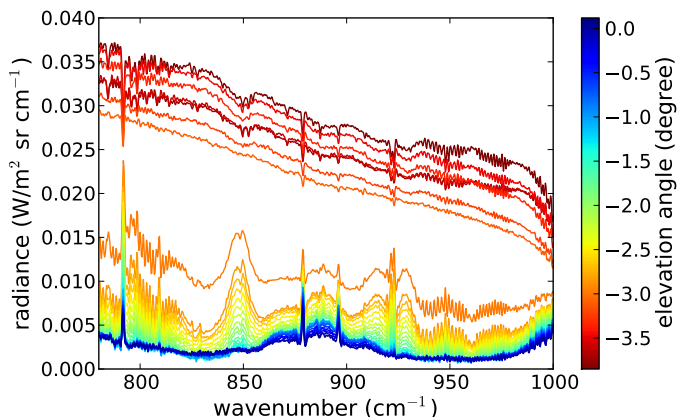


**Figure 5.7:** ESSenCe: Spectra for various heights from profile 70. Prominent signatures are the  $\text{CO}_2$  Q-Branch at  $792.5 \text{ cm}^{-1}$ , the emission from CFC-11 at  $850 \text{ cm}^{-1}$  and that from  $\text{HNO}_3$  at  $890 \text{ cm}^{-1}$ . Spectra from lower elevation angles show the broadband emissions from clouds.

## 5.3. Retrieval Results and Validation

Due to technical difficulties with GLORIA during its first campaign, only a short dynamics mode sequence is usable. This sequence was taken during the second flight and consists of 121 images or 8703 spectra (after cloud filtering). These profiles are used for the following discussion.

For the error analysis, retrieval results of profile 70 from the middle of the sequence were used. This profile was measured at 15:04:49 UTC at  $67.44^\circ \text{ N}$ ,  $7.33^\circ \text{ E}$ . Figure 5.7 shows limb radiance values for this profile, from which our retrieval processor recovers temperature and mixing ratios for  $\text{O}_3$ ,  $\text{HNO}_3$  and CFC-11 as seen in Figure 5.8.

### Error budget

In the error budget, inaccuracies introduced by other trace gases, instrument noise, gain errors, and uncertainty in elevation stability are considered. Table 5.2 shows the values used in the analysis. Instrument noise and gain were estimated to be  $\approx 26.51 \text{ nW}/(\text{cm}^2 \text{ cm}^{-1} \text{ sr})$  and 2% during calibration. Noise characteristics of the detector and the amplifier

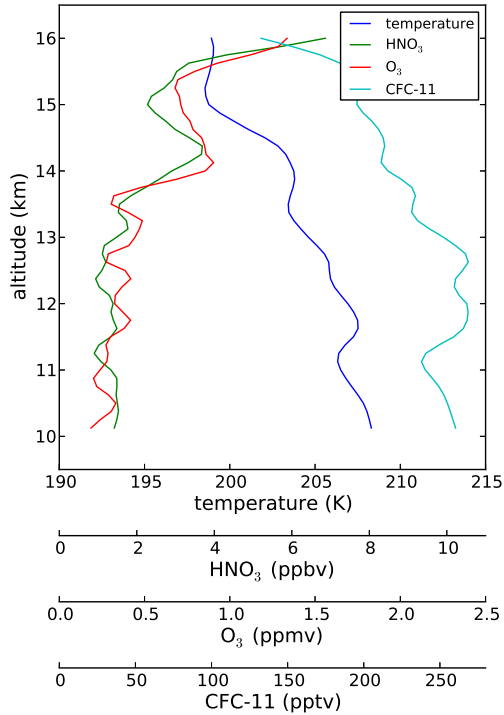


**Figure 5.8:** ESSenCe: Retrieval results for profile 70. Ozone and nitric acid show a correlated increase at 14 km altitude.

can be translated into radiance. Calibration yields an estimation of the noise, which is consistent with these values. The error of the spectral line data from HITRAN is estimated to be  $\approx 5\%$  as described by *Ungermaann* (2013).

The elevation stability can be verified by observation of the cloud top directly in the interferograms. In an ideal Michelson interferometer, half of the total incoming radiation reaches the detector unmodulated. If clouds are in the line of sight, the measured radiance increases sharply, often by a factor of two or more. At some distance from the zero crossing, the baseline is much stronger than the modulation and a gradient can easily be detected. Assuming that the cloud top height does not change quickly, e.g. within one interferogram, the apparent cloud top is a proxy for the pointing stability.

Default	Std. deviations from MIPAS reference atmospheres
Temperature	1 K
Pressure	0.3% of the climatological mean
PAN	100% of value
Instrument noise	$26.51 \text{ nW}/(\text{cm}^2 \text{cm}^{-1} \text{sr})$
Gain	2%
Elevation stability	$0.023^\circ$
Spectral line data	5%

**Table 5.2:** Error estimates for the retrieval depending on instrument and atmospheric situation

The combination of noise and gain limits temperature to a precision of 1.5 K in common 1-D retrievals without horizontal regularisation. The gain error is a systematic error caused by uncertainties in the calibration. Main contributors were the uncertainties in the black body temperature and the unknown behaviour of the detector. The application of horizontal regularisation can significantly improve the error induced by noise. The temperature error can be reduced to 0.5 K (Figure 5.9a). The leading error terms for this temperature error are gain and uncertainties in  $\text{CO}_2$  volume mixing ratio. Errors in the trace gas retrievals are dominated by instrument noise and pointing uncertainty (Figures 5.9b-5.9d).

Figure 5.10 shows the vertical resolution of profile 70. It is best for

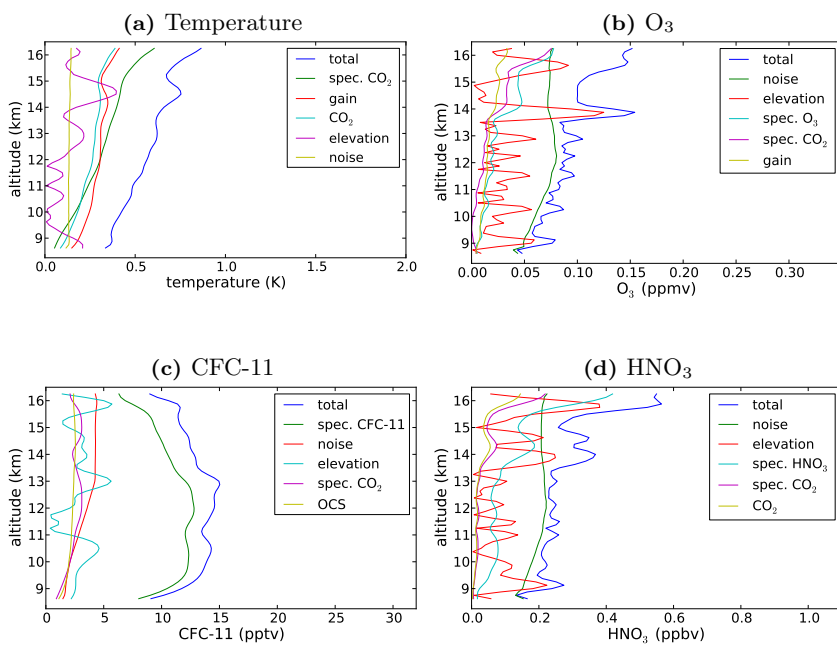


**Figure 5.9:** ESSenCe: Error analysis for profile 70. Retrieval results are shown in Figure 5.8

$\text{HNO}_3$  and  $\text{O}_3$  with a resolution of 300 m to 500 m. Stronger regularisation is necessary for temperature, which limits the achievable resolution. In the case of CFC-11 and CFC-12, the resolution is best near the aircraft and deteriorates at lower altitudes. This effect is caused by the opaqueness of the associated microwindows. The microwindow must be transparent to allow light from the lower altitudes to be transmitted to the detector.

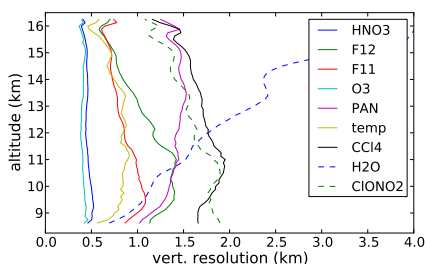
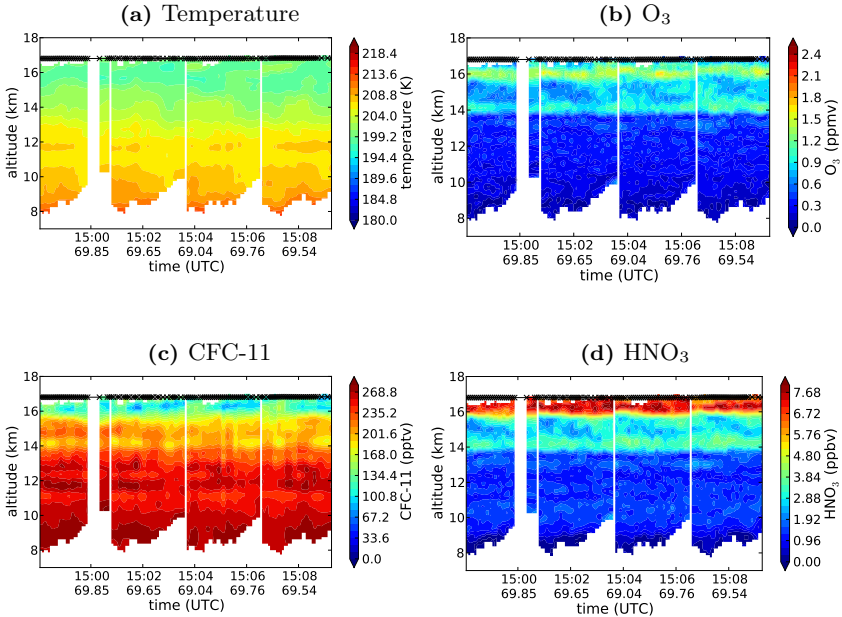


Figure 5.10: ESSenCe: Vertical resolution for profile 70

## 2-D distributions of measured species

The results of the GLORIA retrievals are shown in Figures 5.11 in a 2-D cross section view. The profiles are ordered by measurement time. Four swaths were completed during the sequence. Each swath overlaps about  $3/4$  with the next and previous one. Overall the atmospheric situation was horizontally very homogeneous. At 14 km a continuous layer of high ozone and nitric acid can be seen, which are both abundant in the stratosphere and have low concentrations in the troposphere.  $\text{HNO}_3$  and  $\text{O}_3$  are produced mainly in the stratosphere. In the troposphere, they are both by-products of pollution, but they are usually confined to the boundary layer. Thus, high values are a sign that the air masses originate from the deeper stratosphere. Between 14 and 16 km there is a region of low stratospheric tracers. CFC-11 is a pollutant used as a non-reacting gas in vapour-compression refrigeration. It is destroyed in the stratosphere by UV light and releases chlorine, which is a key contributor to the formation of the polar ozone hole. Because CFCs are released at ground level, their mixing ratios are higher in tropospheric air. Although

at this altitude the gradient is still quite weak, CFC-11 is anti-correlated to the ozone and nitric acid as expected.



**Figure 5.11:** 2-D cross sections of temperature and volume mixing ratios of retrieved species. A thin filament with high ozone and nitric acid values is visible at an altitude of 14 km. Low values in CFC-11 are present at the same altitude.

## 5.4. Validation

For validation purposes, GLORIA results were compared with several other instruments. Profiles from the satellite experiments Envisat MIPAS and EOS Aura MLS (Microwave Limb Sounder) were available. Since the horizontal sampling of these instruments is relatively coarse compared to GLORIA, the average of all GLORIA profiles is used for comparison. Additionally, the GLORIA profiles were folded with the respective satellite averaging kernel. Collocations between our measure-

ments and the satellites can be seen in Figure 5.12. The horizontal resolution of Envisat MIPAS is  $\approx 30$  km across the line of sight and  $\approx 300$  km along the line of sight (*von Clarmann et al.*, 2009). The horizontal resolution of Aura MLS is 7 km to 210 km (*Read et al.*, 2007). The MIPAS-STR instrument has excellent collocation, because it was mounted on the same platform and had the same measurement direction. No additional averaging kernel is applied for comparison with MIPAS-STR.

The closest radiosonde was launched at Bodø, Norway and is included for comparisons of temperature. During ascent and descent of the aircraft, measurements of CFC-12 and temperature were taken by in situ instruments. The aircraft itself included a system for temperature measurements. The High Altitude Gas Analyzer (HAGAR) is a spectrometer which can measure halogen compounds such as CFC-11. The Whole Air Sampler (WAS) stores air samples in evacuated canisters which can later be analysed with laboratory equipment.

Instrument	Products used
Envisat MIPAS	Temperature, O <sub>3</sub> , HNO <sub>3</sub> , CFC-11, CFC-12
MIPAS-STR	Temperature, O <sub>3</sub> , HNO <sub>3</sub> , CFC-12
EOS Aura MLS	Temperature, O <sub>3</sub>
Radiosonde	Temperature
HAGAR	CFC-11, CFC-12
WAS	CFC-11, CFC-12

**Table 5.3:** Instruments used for validation

## Temperature

All temperature measurements seem to be in good agreement, even considering the sometimes rather large distance between collocations (Figure 5.13). ECMWF, the radiosonde, and UCSE all show a similar temperature profile. The on-board temperature measurements (UCSE) were taken during ascent and descent over Sweden. Only MIPAS Envisat shows a slight warm bias. All satellites had difficulties at this low altitude due to high aerosol load and PSCs. This increases their uncertainties significantly. Measurements from MIPAS-STR and GLORIA were taken from the same air volume. As expected, the agreement is very

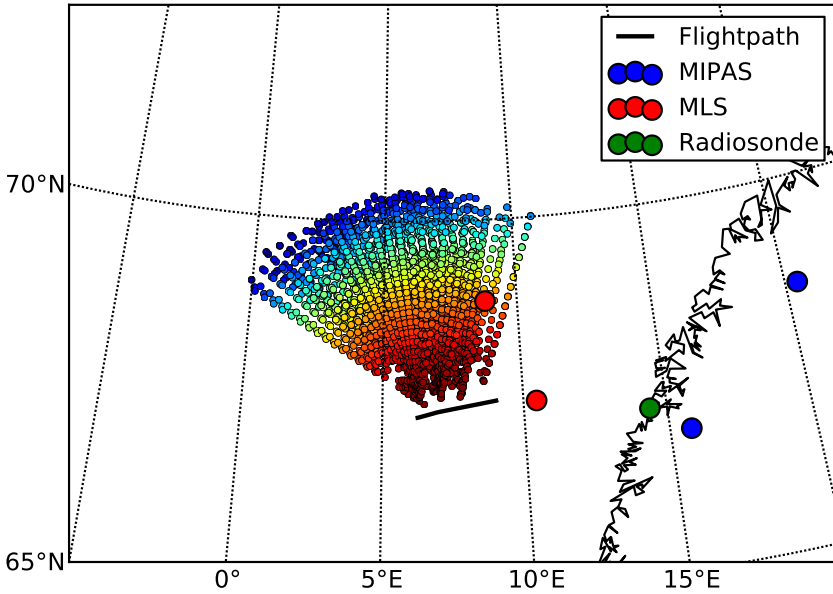


**Figure 5.12:** GLORIA tangent points and locations of other measurements used for validation

good (within 1 K, Figure 5.18a).

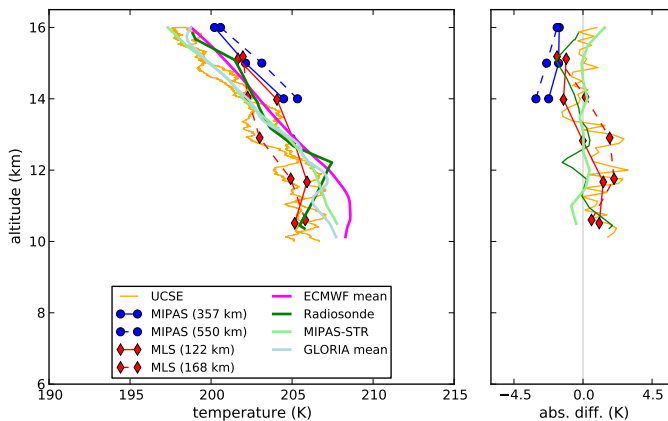


**Figure 5.13:** Absolute differences of temperature between GLORIA and other instruments

## Nitric acid

The GLORIA retrieval results (Figures 5.14 and 5.18c) are in overall good agreement with MIPAS-STR, apart from the structure between 14 km and 16 km. It is, however, possible for MIPAS-STR to miss these changes due to the poorer vertical resolution of 1 – 1.5 km. A very strong regularisation was used in the MIPAS-STR retrievals (Woiwode, pers. comm.). MIPAS Envisat seems to show too large values for  $\text{HNO}_3$ .

## Ozone

A similar result can be seen when comparing ozone data with satellites (Figure 5.15). The GLORIA retrievals underestimate the mixing ratio of  $\text{O}_3$  slightly. The agreement with MIPAS-STR data (Figure 5.18b) is better, up to 13 km altitude. The differences between 14 km and 16 km may be due to the influence of clouds on the measured spectra. Both  $\text{HNO}_3$  and  $\text{O}_3$  are correlated in GLORIA data, which is to be expected because both are stratospheric tracers.

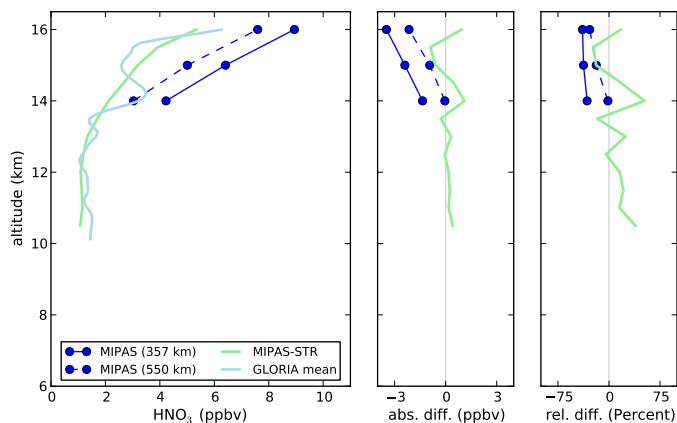


**Figure 5.14:** Absolute and relative differences of nitric acid between GLORIA and other instruments

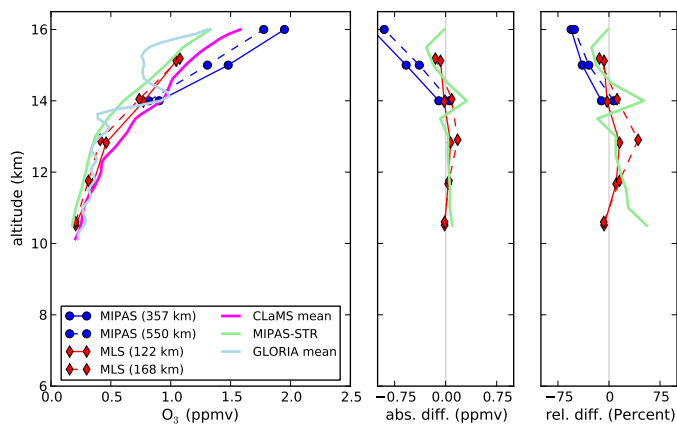


**Figure 5.15:** Absolute and relative differences of ozone between GLORIA and other instruments

## CFC-11 and CFC-12

Measurements taken in situ are in very good agreement with model data, which is expected as CFC-12 is well mixed in the troposphere. GLORIA slightly overestimates the concentration of CFC-12 in comparison to these profiles (5%, Figure 5.16). Only Envisat MIPAS data is available for this trace gas. The two profiles from MIPAS show a significant split, which may again be related to the aerosol conditions. Significant differences between MIPAS-STR and GLORIA arise in CFC-12. Figure 5.18d also shows an overestimation. There is a slight drop in mixing ratios visible at 14 km, which is correlated between the two instruments.

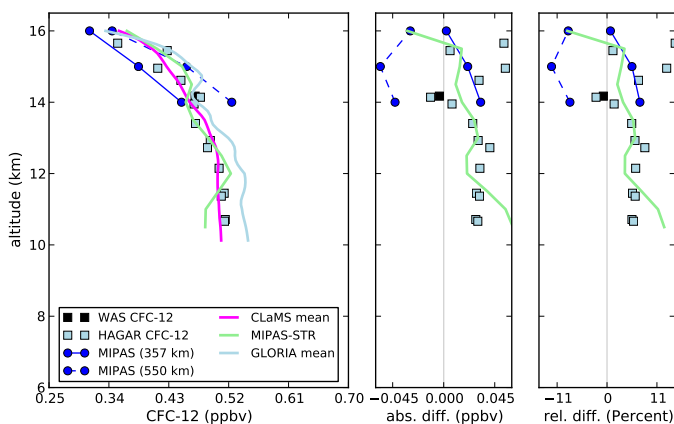


**Figure 5.16:** Absolute and relative differences of CFC-12 between GLORIA and other instruments

CFC-11 retrieval shows similar results as CFC-12. Overall CFC-11 is overestimated, although it shows the same relative structure at 14 km as MIPAS-STR.

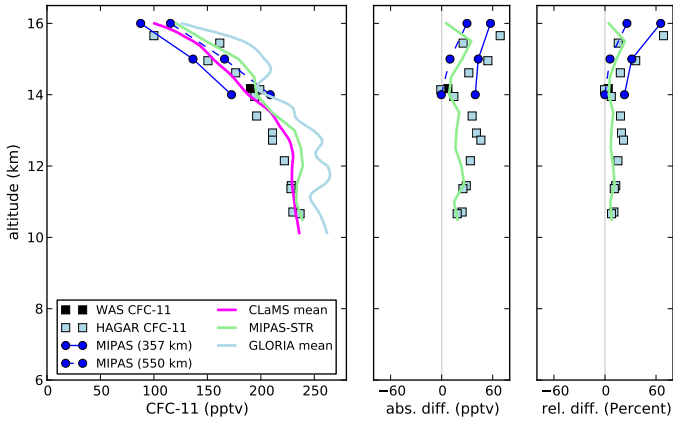


**Figure 5.17:** Absolute and relative differences of CFC-11 between GLORIA and other instruments

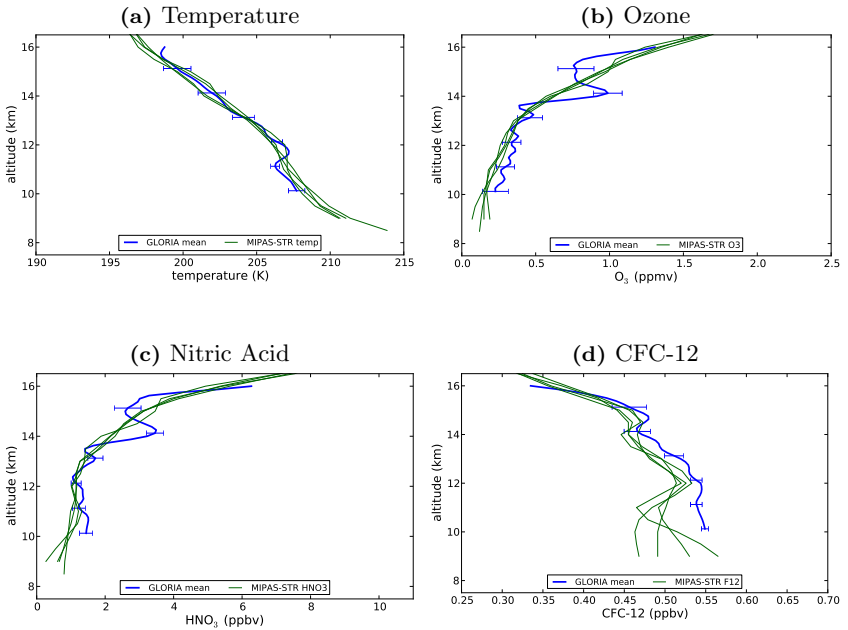


**Figure 5.18:** Comparison between MIPAS-Str and the mean GLORIA profile

## 5.5. Chapter Summary

The very cold temperatures measured by GLORIA were consistent with in-situ data and satellite measurements. Above the flight altitude, MIPAS Envisat shows the presence of polar stratospheric clouds (PSCs). While NAT particles may not form at the flight level, they can cross this altitude without evaporating. The additional nitric acid at 14 km may be deposited there by sedimentation.

The Chemical Lagrangian Model of the Stratosphere (CLaMS, *Grooß et al.*, 2002) can be used to analyse the trajectories of air parcels by simulating their movement with ECMWF wind data. An analysis of the past position of the measured air parcels shows that air above 11 km altitude did not leave the polar vortex in the previous 10 days (Figure 5.19). Air parcels below this altitude originate from above Siberia and the Northern Pacific. The ECMWF dataset sets the tropopause altitude at 9.5 km, which coincides with the measured cloud top height. Below the tropopause, the polar jet does not function as a transport barrier.

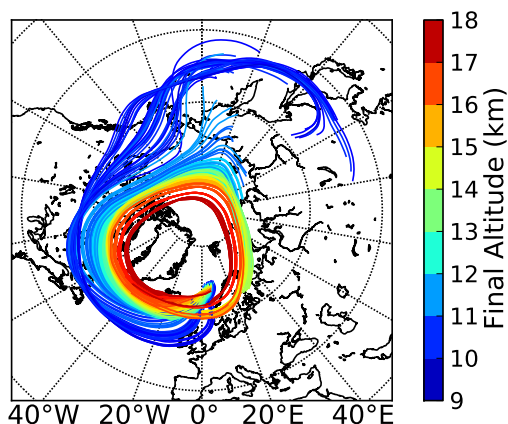


**Figure 5.19:** CLAMS 10 day backward trajectories with the GLORIA tangent points as end points. Colours mark the final altitude of the air parcel.

Although the first campaign of the GLORIA instrument suffered from various technical problems, it showed that the instrument concept is valid. The part of the flight time which yielded usable measurements still

generated promising results. The conditions inside the polar vortex were very homogeneous and the test flights could not be planned to include very strong gradients. The data still contains an interesting feature, which is hard or impossible to see with the established remote sensing instruments.

It also provides a good test case for the automatic spectral window selection. All selected targets are covered by spectral windows. The chosen windows are similar to the selection a person experienced in infrared sounding would choose for this situation. Unfortunately, not all targets yield usable information. Water vapour is an important trace gas, but difficult to derive in the spectral range used in this evaluation. The derived profiles are not physically plausible, because of the data quality issues. The targets shown here are, however, well within the expected range of quality.

## 6. Parallel Retrievals in JURASSIC

One of the most important insights in high performance computing in the last years was: "The free lunch is over" (*Sutter, 2005*). The performance of a single central processing unit (CPU) no longer rises exponentially. To maintain the same level of performance increase as in previous years, more and more computational cores must be packed into each CPU. To harness the power of these cores, a shift in programming must be made, from serial computation to concurrency. The demands of 3-D retrieval are far beyond the capabilities of serial processing and must be done in parallel.

There are many different models for parallelisation. A common distinction is made along the memory model. If different strands of execution, commonly called threads, have access to a common memory range, this is called the shared memory model. The OpenMP compiler extension follows this model. Multiple threads are generated by annotating the source code with special commands. Division of work is automatically done by the runtime library. On common, hardware this approach is limited to running on a single computer. When multiple computers are involved, the distributed memory model has to be used. One implementation of this is the Message Passing Interface (MPI). Different processes no longer access the same memory, but exchange information by passing messages between them. MPI is a software library which facilitates this communication. The division of work must be done manually.

Different parallelisation approaches can also be classified by the distribution of control. In this work the master-slave principle is used. The master process controls the retrieval and gives orders to the clients, which returns the result of their calculations to the master. A complete picture

of the current state of the system is held by the master, making decisions about program flow very easy. This system fails if the global state becomes too large for a single node to handle.

The first implementation of 3-D tomography by *Ungermann et al.* (2010b) was developed to work with a single trace gas and a coarse atmosphere representation. Although an OpenMP parallelisation was implemented, it was inherently limited by the memory size of a single node. Since then, significant improvements in performance were implemented. A first major speedup is achieved by changing the calculation method of the Jacobian matrix. With aid of the STCE (Software and Tools for Computational Engineering) group of RWTH Aachen University, an adjoint solution based on expression templates (*Veldhuizen, 1995*) was developed in the course of this thesis and is used operationally in JURASSIC. Several features of the adjoint code have now been incorporated into the tool of the STCE, which is also supported

An adjoint model is an algorithmic method for computing an exact gradient of a function. During function evaluation, partial derivatives of sub-functions are stored in a data structure called "tape" and are later multiplied together to evaluate the gradient. This can be used to recover the Jacobian matrix. A short description of algorithmic differentiation and adjoint models is given in appendix D. The adjoint model provides a speedup of two orders of magnitude in comparison to the previously used finite difference model. This radically changed the relative runtime of kernel computation and linear algebra. While previously the total time was clearly dominated by the former, while with the adjoint model the two are about equal. To achieve further performance improvements, the linear algebra module needs to be optimised, too.

## 6.1. Parallelisation of JURASSIC

The retrieval contains two distinctive parts with different requirements for parallelisation. Forward model evaluation and subsequent kernel calculations are embarrassingly parallel problems, because each pencil beam only depends on the input atmosphere and can be calculated without information from other pencil beams. In contrast, the linear algebra needed for minimisation consists primarily of matrix-vector products, which require much more frequent synchronisations between different threads and

processes.

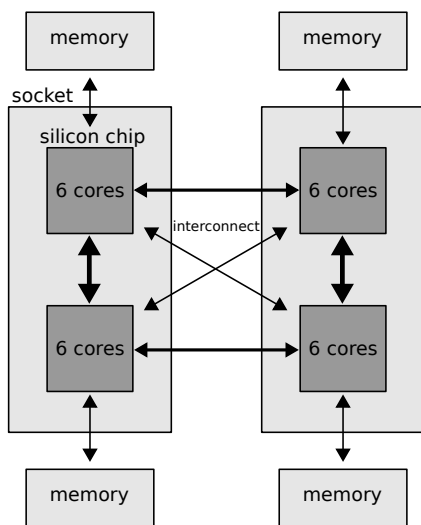


**Figure 6.1:** Example of a modern NUMA system: the AMD Magny-Cours system with 24 cores on 2 sockets with 4 chips and 6 cores each.  $1/4$  of the main memory is attached to each chip. Access to non-local memory must be gained via interconnects. These fast links have variable speeds, with the connection between two chips on one socket being the fastest.

The speedup obtained by an OpenMP parallelisation depends heavily on the number of threads and the underlying computer architecture. In a non-uniform memory access (NUMA) system (Figure 6.1), a core cannot access the whole memory with the same speed and latency. Some parts of the memory are attached to other cores and must be accessed over a connection between cores. On processors with NUMA, JURASSIC experiences slowdown of up to 50% when atmosphere or table data is located in non-local memory or a thread is moved to another core and access to the working set is no longer local.

To alleviate the scaling problem and extend the parallelisation to use more than one node, we implemented a distributed parallelisation using the message passing interface (MPI). Similar to OpenMP, we distribute pencil beams on MPI processes. Communication is only required to distribute the input state and gather the results. While this solution

does not suffer from scaling issues due to non-local memory, it has a problem with total memory usage. As the different processes can no longer share static data, the size of tables and atmosphere data can quickly become a limiting factor. Table 6.1 shows that the base memory usage for a medium sized 3-D tomographic retrieval is around 3 GiB (gibibyte =  $2^{30}$  bytes). This quickly exhausts main memory on a 24 core machine.

As atmosphere data clearly dominates, two possible solutions present themselves: spatial decomposition of the atmosphere or shared memory parallelism on top of MPI. The fact that OpenMP code was already present led to the decision to implement a hybrid OpenMP/MPI parallelisation.

Tables	$\approx 300$ MiB
Atmosphere	$2 \cdot 10^6$ points $\cdot$ 16 byte $\cdot$ 4 datasets $\cdot$ 22 emitters = 2685 MiB
Measurements	$3 \cdot 10^5$ observations $\cdot$ 16 byte $\cdot$ 4 datasets = 18 MiB
Kernel	$\approx 173$ GiB

**Table 6.1:** Typical memory usage for a 3-D tomographic retrieval. One value takes 16 byte due to adjoint code. Datasets include a priori data and working sets

## Message passing interface

The JURASSIC retrieval processor is driven by running the implementation of a minimisation algorithm, in this case the Levenberg-Marquardt algorithm, on a cost function, which provides general interfaces to the forward model and the data. To keep the general framework intact, the MPI parallelisation is implemented as a master-slave configuration. Each process reads the input file on its own, but only the master process begins processing, all slave processes start listening for commands. It is important that replicated data, such as the atmosphere representation, stays in sync on all processes. This works by performing all accesses through a proxy method which transmits all changes to the clients. Forward model evaluations were implemented by distributing a list of pencil beams to all processes and gathering the results.

The master process still does some administrative work like adding the derivatives for instrument parameters and switching the slaves into

kernel computation mode. The kernel is computed by distributing the pencil beams among the processes and collecting the resulting matrices locally. To handle memory allocations better, the kernel is not stored in one huge data structure, but in multiple smaller objects, each allocated independently. This makes it much easier to grow the allocated memory as needed. The kernel may then be collected at the master process for smaller problems or stored in a distributed manner.

To handle large kernel matrices, the matrices are partitioned over the processes during kernel calculations. To perform matrix-vector products, the input vector is distributed over MPI and the result is gathered after each process has finished its multiplication.

## 6.2. Linear Algebra

One of the most time-consuming tasks is the calculation of diagnostic information on 3-D tomographic retrievals. The gain matrix  $\mathbf{G}$  from Eq. 4.0.1 is needed to derive diagnostic values. This matrix is usually dense and can only be computed and stored for small problems. We can, however, calculate a single line of  $\mathbf{G}$  by solving a linear equation system (Nolet, 1985). Instead of inverting  $\mathbf{M}$ , we solve  $\mathbf{M}\mathbf{x} = \mathbf{b}$  with  $\mathbf{b} = 0$  for all but one entry, which is set to one.

$$\mathbf{M}^{-1} = (\mathbf{S}_a^{-1} + \mathbf{F}'(\mathbf{x})^T \mathbf{S}_\epsilon^{-1} \mathbf{F}'(\mathbf{x}))^{-1} \quad (6.2.1)$$

With a single line  $row_i(\cdot)$ , we can calculate the noise-induced measurement error  $\mathbf{S}_N$  and the averaging kernel matrix  $\mathbf{A} = \mathbf{G}\mathbf{F}'(\mathbf{x})$  from  $\mathbf{M}$

$$row_i(\mathbf{G}) = row_i(\mathbf{M}^{-1})\mathbf{F}'(\mathbf{x})^T \mathbf{S}_\epsilon^{-1} \quad (6.2.2)$$

Matrices are stored in the compressed storage row (CSR, e.g. Bai, 2000) format, which only stores non-zero entries, indexed by row and column. This storage format requires special methods for optimisation. Modern processors provide several mechanisms to improve performance of numerical algorithms, in this case the matrix-vector product. Single instruction multiple data (SIMD) instructions like the Streaming SIMD Extensions (SSE) can be used to performance multiple arithmetic operations at once on different words.

Normally, data fetched from the main memory is stored in a smaller, but faster cache for immediate reuse. Special “prefetching” instructions exist to declare data non-temporal (not reused in the near future), which should not be stored in the processor cache infrastructure. These instructions can be used to load matrix entries, which generally do not fit into the cache as a whole. This avoids filling the caches with data which would be evicted before it could be reused. Loops always contain some overhead, e.g. to keep track of the round trip. This can be made more efficient by performing more than one calculation in the loop body.

All of these techniques are heavily dependent on the hardware the algorithm runs on. Thus a program was created to test multiple combinations and select the fastest. Figure 6.2 shows the result of an optimisation run for the matrix-vector product with a transposed matrix in CSR format. If loop unrolling is done too often performance decreases again. This benchmark was performed on an empty node, making the effect of memory prefetching visible. If the memory bandwidth is saturated, prefetching loses efficiency.

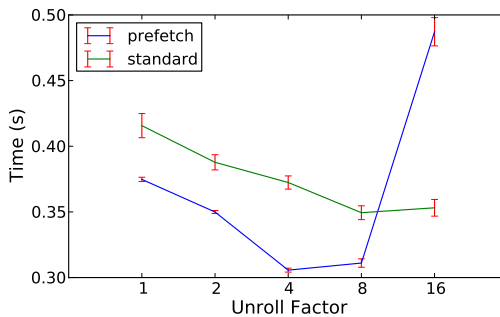


**Figure 6.2:** Results of automatic performance optimisation for linear algebra. Algorithm: Matrix-vector product in CSR format with transposed matrix. Unrolling and memory prefetching applied. Standard deviations increased 10x for visibility.

An additional optimisation is implemented for the diagnostics calculations. Usually not only one row of  $\mathbf{G}$  is calculated. Performance can be easily improved in the matrix-vector product if the matrix data can be used more than once per load operation. Instead of only using one right side, the equation is solved for multiple right sides. In this way multiple diagnostic values can be calculated simultaneously. Multiplication with

eight vectors is implemented in JURASSIC. Compared to a single vector, multiplication an overall speedup by a factor of four is achieved.

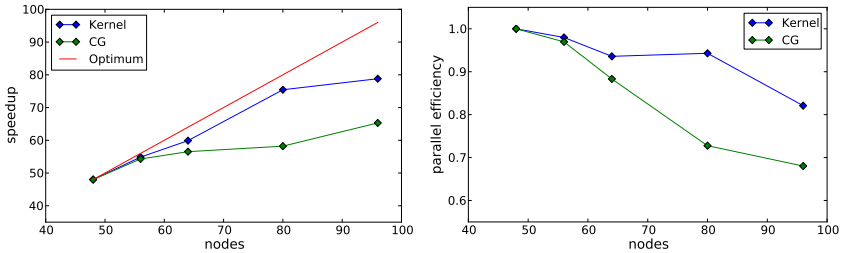
## 6.3. Parallel Efficiency

While the main purpose of the parallelisation efforts is to enable retrieval of very large datasets, we tried to maintain good parallel efficiency as well. The speedup of a parallel program is defined as the relation between the time of execution on a single node  $T_1$  and  $p$  nodes  $T_p$ :

$$S_p = \frac{T_1}{T_p} \quad (6.3.1)$$

Ideally  $S_p = p$ , although in practice no algorithm can run in parallel perfectly. For a better understanding, we can look at the parallel efficiency  $E_p$ , which shows the percentage of resources used for calculations instead of overhead.

$$E_p = \frac{S_p}{p} \quad (6.3.2)$$



(a) Speedup for hybrid MPI/OpenMP parallelisation (b) Parallel efficiency for hybrid MPI/OpenMP parallelisation

**Figure 6.3:** Analysis of parallel performance for a 3-D tomographic test case

A test case representative of a large tomographic retrieval was derived from the TACTS/ESMVal dataset. It has  $13 \cdot 10^6$  unknowns and 370000 measurements. The measurements consist of profiles with 7 ISW from 871 images taken during a hexagonal flight pattern. The retrieval has 5 targets in a full 3-D atmosphere representation. The kernel size is

# Nodes	# Cores	Kernel (min)	CG (min)
6	48	176.1	942.0
8	64	141.2	800.0
12	96	107.3	692.4

**Table 6.2:** Runtime of the 3-D tomographic benchmark

173 GiB and is stored distributed on all nodes.

The benchmarks are run on two socket nodes with 2.5 GHz quad-core AMD Shanghai processors and 64 GiB memory with Infiniband interconnect between nodes. One MPI process is started per node and uses all cores via OpenMP. As the benchmark is too large to be run on a single node, all calculations are based on the performance on 6 nodes (48 cores).

Kernel calculations are done with the adjoint model and the resulting matrices are stored in a distributed manner. The time taken includes execution of the adjoint model and generation of matrices. The linear algebra part uses this Jacobian matrix to solve a linear equation system used in diagnostics, where we solve for eight right hand sides at once.

The parallel efficiency of the kernel calculations is much better than in the linear algebra part (Figures 6.3). The efficiency loss in benchmarks run on more nodes is caused by a single slow node that was present in each run performed for the benchmark, which stalled the other processes at the end of the run. This was likely caused by NUMA-related placement problems in the kernel. More detailed studies showed that the problems were not associated with a specific set of pencil beams. The diagnostic calculation scales much less favourably. For each matrix-vector product two large vectors need to be transferred, which takes a considerable time even on the very fast Infiniband interconnect.

## 6.4. Chapter Summary

With the improvements introduced in this chapter, the maximum feasible size of 3-D tomographic retrievals is no longer limited by runtime but by memory available for kernel storage. Typical compute nodes routinely have 64 to 128 GiB of main memory. Expansion to multiple nodes is needed to accommodate multi-target tomographic retrievals. The final

runtime of a retrieval depends only partially on processor speed, but to a greater extent on available memory bandwidth, especially during linear algebra.

Even though scaling is currently hindered by NUMA related performance bottlenecks and inherently serial parts in the linear algebra, it is possible to perform retrievals of current 3-D tomographic data sets with a turnaround time of less than two days. Should the need to solve larger problems arise, the speedup remains acceptable as long as the size of the kernel matrix part on each node is sufficiently large.

## 7. 3-D Tomographic Retrieval of an ESMVal Hexagon Flight

The joint TACTS and ESMVal campaigns were the first time that GLORIA was employed on the German High Altitude and Long Range Research Aircraft (HALO, Figure 7.1). The TACTS campaign (Transport and Composition in the UT/LMS) was planned as a series of flights between the home base of HALO in Oberpfaffenhofen and Sal, Cape Verde, with the intention of crossing the subtropical jet multiple times. This was done to study the horizontal exchange between troposphere and stratosphere. In contrast, the ESMVal campaign (Earth System Model Validation) intended to perform measurements with a large latitude coverage to validate atmosphere models.



**Figure 7.1:** The German High Altitude and Long range research aircraft (HALO) on the runway. The GLORIA instrument is mounted in the belly pod.

Scientific flights started from Spitzbergen, Norway, to Cape Town,

South Africa, and from there southwards towards Antarctica. Several of the objectives were achieved from Oberpfaffenhofen without flying to Sal since the subtropical jet shifted to the north. The southernmost flight took place on 12th September 2012, starting from and ending in Cape Town with a total flight time of 9.5 hours. An overview of the flight paths can be seen in Figure 7.2. The southernmost point was at  $65^\circ$  south where, after the turnaround, a dive was performed. On the way back, fuel levels permitted a small hexagon to be flown for tomographic GLORIA measurements.

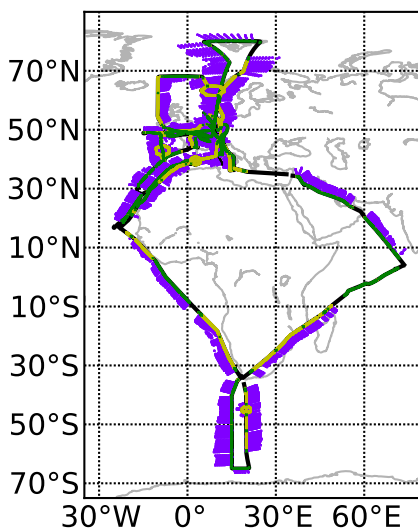


**Figure 7.2:** Overview of all TACTS/ESMVal flight paths. GLORIA chemistry mode measurements are marked in green, dynamics mode is marked in yellow.

## 7.1. Meteorological Situation

The flight towards Antarctica entered the polar vortex before turning around. On the way back to Cape Town, a structure at the edge of the polar vortex was selected as a target for the hexagon. The pattern was at the edge of a high potential vorticity zone that marks stratospheric air masses. Preliminary data gathered by the in situ instruments (pers.

comm.) also indicate that the aircraft crossed a steep ozone gradient twice.

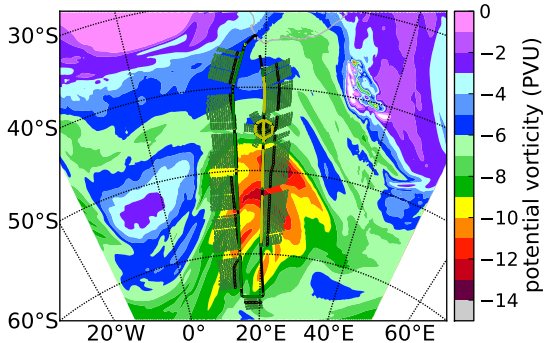


**Figure 7.3:** Overview of the flight path of the TACTS flight on 12th September 2012. Chemistry mode is marked in green, dynamics mode is marked in yellow. The hexagon is located on the way back to Cape Town just north of a zone with high potential vorticity at 12 km altitude.

The ECMWF reanalysis data set provides insights into the meteorological situation through global wind and temperature fields, and potential vorticity (PV), supplemented by trace gas distributions. Figure 7.4 shows the absolute wind speed in the region of the retrieval. Wind speed is very high due to the polar jet. A wind shear of  $10 \text{ ms}^{-1}$  between the southward leg of the hexagon and the lower tangent points in the north is visible in Figure 7.4a. The vertical tilt of the shear is aligned with the stratospheric filament. The shear is caused by the distortion of the jet stream at 10 km altitude. The jet in the lower layers is disturbed by a Rossby wave, but this effect is much less pronounced at 14 km.

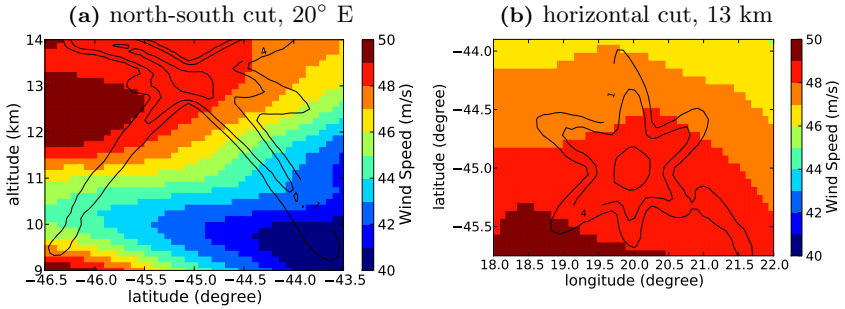


**Figure 7.4:** ECMWF absolute wind velocity. In the area of the hexagon, marked by the thin black lines, a wind shear of  $10 \text{ ms}^{-1}$  was present.

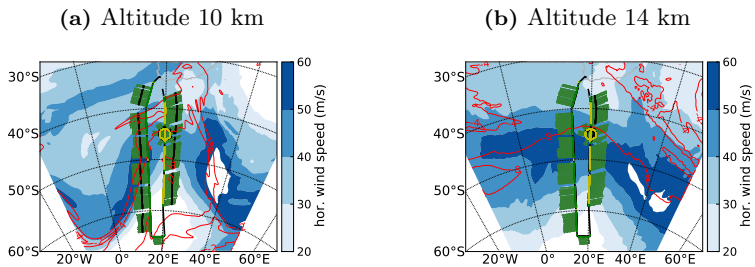


**Figure 7.5:** ECMWF horizontal wind velocity at synoptic scale. Red contour lines show potential vorticity. Flight path shown in yellow for dynamics mode and green for chemistry mode.

## 7.2. Retrieval Setup

The retrieval atmosphere is defined on a 3-D grid that was automatically generated to match measurement data. Geometric tangent points were calculated for all measurements and a grid with a minimal horizontal grid spacing of 7.5 km was generated to include them. Outside of the central region, the grid was extended to cover all lines of sight, but with increasing grid spacing. A vertical grid spacing of 125 m, which is slightly finer than the GLORIA sampling, was chosen for the altitude range from 5 to 20 km with reduced sampling density below and above up to a top altitude of 60 km. This results in a grid of  $2.1 \cdot 10^6$  points.

The microwindows used for the retrieval were chosen by applying the method from Chapter 4. The algorithm produced seven microwindows for the retrieval of temperature, ozone, nitric acid CFC-12 and water vapour and two aerosol profiles as secondary targets. In contrast to ESSenCe, the spectrometer was run at  $0.6250 \text{ cm}^{-1}$  spectral sampling and  $\approx 1.2 \text{ cm}^{-1}$  spectral resolution. Raw data was converted to radiance data based on two black body measurements.

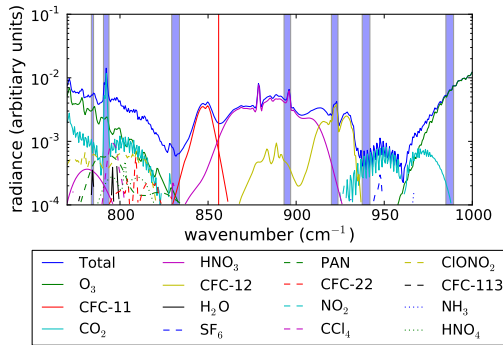


**Figure 7.6:** Locations of microwindows in the spectrum

Only data from pixels with a geometric tangent point between flight altitude (no upward looking measurements) and 9 km was used for the retrieval. Although the air was essentially cloud-free (Figure 7.7), the lower altitudes were excluded from the retrieval, because the high water vapour mixing rates in the troposphere influence the retrieval negatively. The pencil beam grid was set up with one beam per pixel in the vertical

Microwindow			bit	
783.750	-	785.000	H <sub>2</sub> O	13.6
790.625	-	793.750	temperature	29.4
829.375	-	833.750	aerosol 1	28.3
893.125	-	896.875	HNO <sub>3</sub>	68.5
920.000	-	923.750	CFC-12	27.2
937.500	-	941.875	aerosol 2	55.3
985.000	-	989.375	O <sub>3</sub>	48.1

**Table 7.1:** Microwindow selection for 3-D tomographic retrieval

direction instead of oversampling the detector as done in 1-D retrievals to reduce memory usage.

While the horizontal field of view has not yet been measured (see the vertical FOV in Figure 7.8), its approximate half width can be calculated on the assumption that the shape is Gaussian. The instantaneous field of view of 48 pixel is  $1.5^\circ$ . At the 10 km tangent point, this is about 6.6 km horizontally. This is less than the horizontal resolution of the grid. A finer sampling does not significantly increase the resolution of the retrieval result.

A priori profiles for most trace gases were taken from the MIPAS reference atmospheres. For pressure, temperature, and water vapour, the ECMWF reanalysis data set was used. Other model sources were not available. From 1-D retrievals a small pointing bias of  $0.1^\circ$  was derived for the complete flight and corrected for.

## 7.3. Retrieval Results

The retrieval was executed using the hybrid MPI/OpenMP parallelisation in JURASSIC. The total runtime was 1550 min on 40 cores and the kernel matrix used 122 GiB of memory.

Figures 7.9a - 7.10d show the retrieval results for all targets. For each target a horizontal cut at 13 km and a vertical cut in east to west directions at  $20^\circ$  east is shown. The tangent points form a parabolic shape, which can be seen in the vertical cuts. At 13 km the tangent points of measurements taken from the opposing sides of the hexagon coincide at the same horizontal position. In the middle of this area, measurements

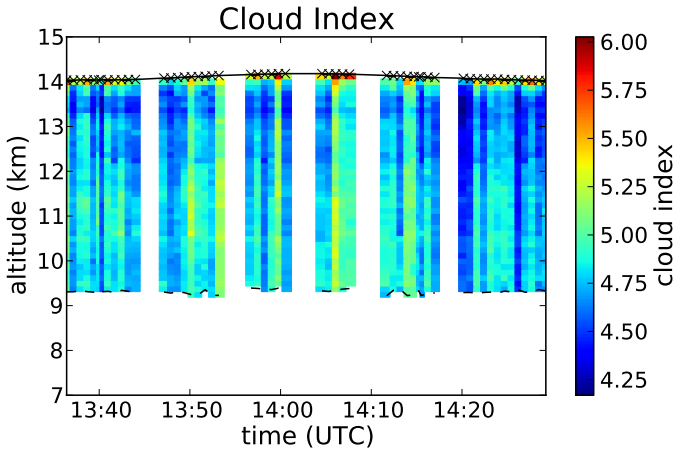


**Figure 7.7:** Cloud indices for the hexagon near Antarctica. Only measurements perpendicular to the flight direction are shown. High values indicate higher transparency. Values below 4 are assumed to be cloudy.

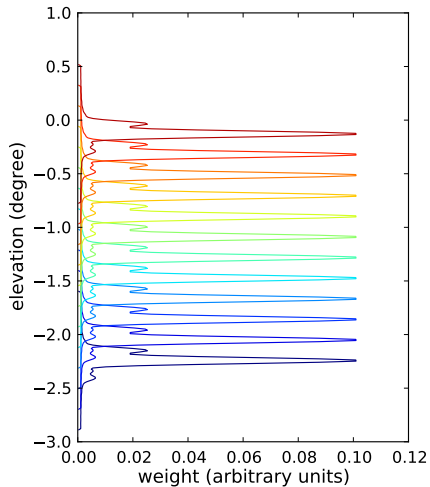


**Figure 7.8:** Vertical field of view of every 6th pixel of the GLORIA detector. The side lobes are caused by reflections on the beam splitter.

from all directions contribute to the result and the tangent point density reaches about 70 points per grid cell. In this region, tomographic theory implies that stable results can be expected.

A filament of air containing a high nitric acid and ozone concentration with a vertical extent of around 500 m is located within the measurement region. This filament is anti-correlated with CFC-12. In the horizontal dimension, a ring of high ozone and nitric acid is visible, which seems to extend downward along the lines of sight to the lower tangent points. These are artefacts that are likely caused by horizontal inhomogeneity outside of the stable region that cannot be properly resolved. All of the effects are, however, outside the stable region. Figure 7.10c shows an influx of high water vapour from the south.

A first estimate of the retrieval's apparent resolution can be derived from the filament. To be able to show a filament of 500 m in extent, the resolution must be 500 m or better. The same holds true for the horizontal extent of about 30 km.

For our retrieval, the most valuable product of the ECMWF data set is the temperature. As already described, it is used as a priori information for the regularisation of the retrieval. The retrieval yields some differences to ECMWF as seen in Figure 7.11. There is a slight high bias of up to 0.5 K in the stable region. The larger negative bias above and below the stable area corrects for temperature variations along the rest of the line of sight, as the values farther away quickly regress to the a priori due to the regularisation.

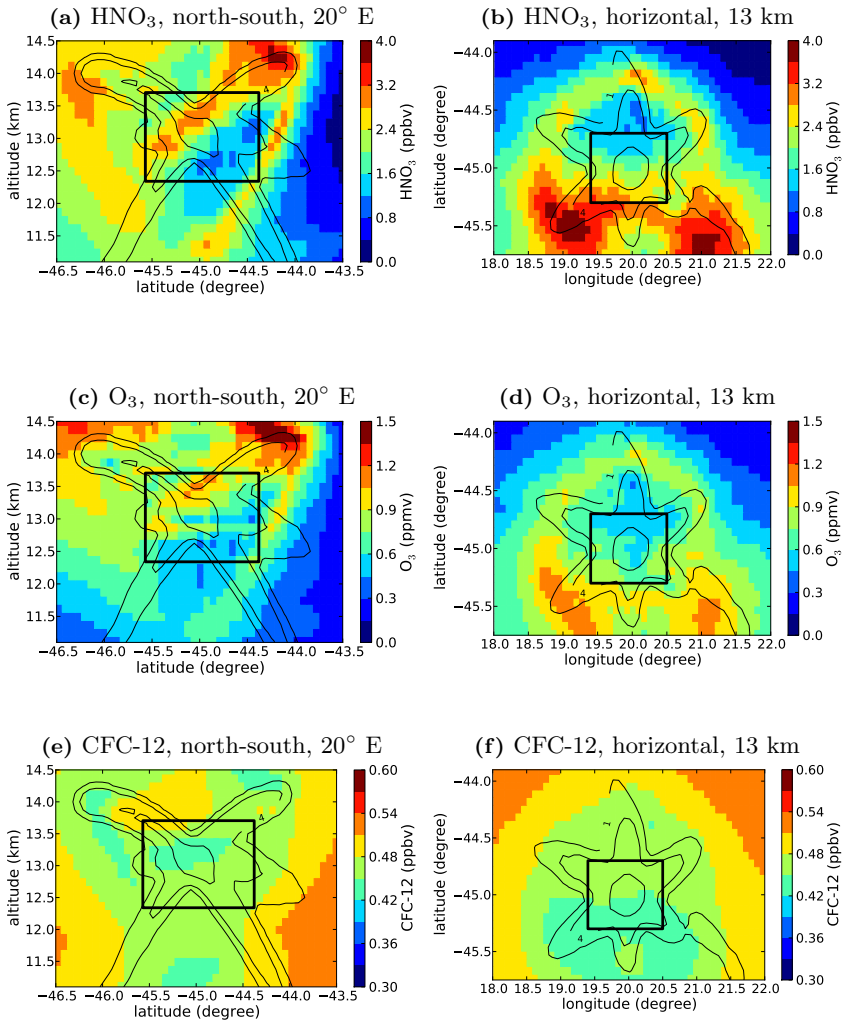


**Figure 7.9:** Retrieval results for 3-D tomographic retrievals. Thin black lines show the density of tangent points. The thick black rectangle marks the region with measurements from all angles. North-south cut at  $20^\circ \text{ E}$ , horizontal cut at 13 km.

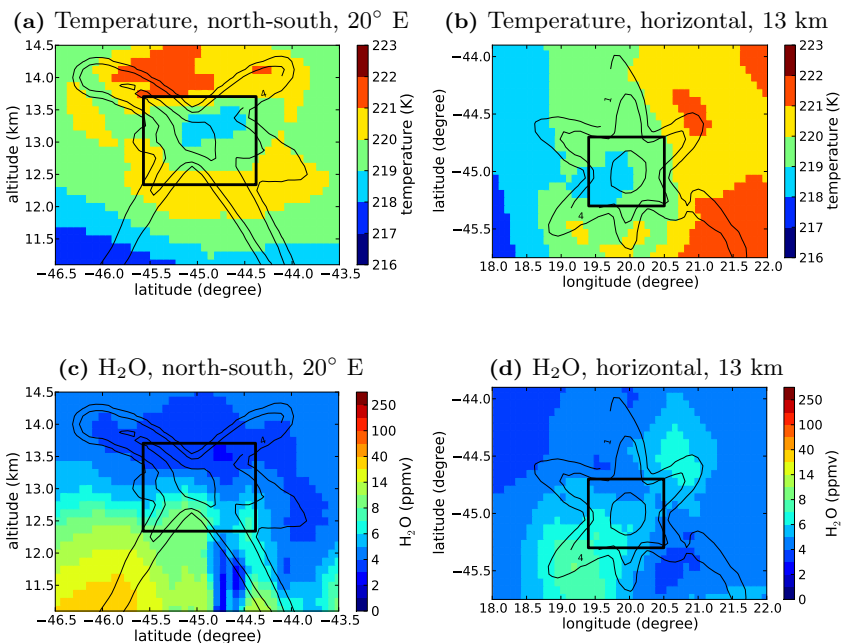


**Figure 7.10:** Retrieval results for 3-D tomographic retrievals. Thin black lines show the density of tangent points. The thick black rectangle marks the region with measurements from all angles. North-south cut at 20° E, horizontal cut at 13 km.

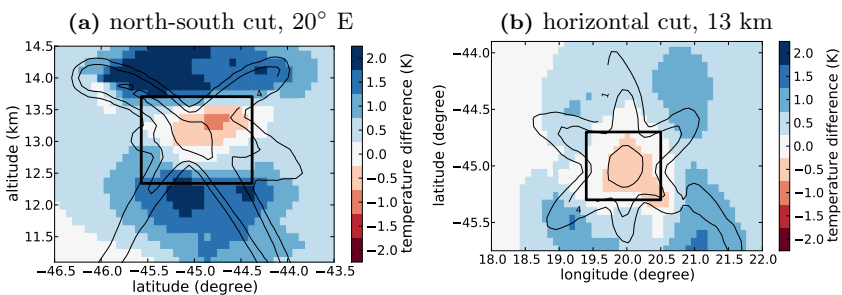


**Figure 7.11:** Absolute difference between retrieval and ECMWF temperature

## Error budget

Most of the considerations done for ESSenCe (Section 5.3) are also valid for the analysis of TACTS and ESMVal data. The most important change was that the corner cubes were improved and no longer induced a velocity shift in the interferograms. It was also possible to use two black bodies for calibration, which enables the use of all spectral region in the regions accessible by GLORIA.

A 1-D retrieval with horizontal regularisation was done to obtain an estimate of the error budget (Figure 7.12). A full error analysis can currently not be done with a 3-D retrieval. Several minor trace gases were omitted in the 3-D retrieval setup and in the 1-D retrieval. The errors shown in Figure 7.12 could therefore be reduced by including them.

For the hexagon only a limited amount of validation measurements was available. While the aircraft had several in situ instruments on board, all measurements in the vicinity are on the flight level. Measurements from the dive and from the start and landing are from different meteorological situations. Unfortunately, the flight level was out of the stable region of the 3-D tomographic retrieval and thus of little use.

The volume mixing ratios for CFC-12 are well known at low altitudes. Because it is well mixed, the gradients are usually very low in the regions GLORIA can measure from HALO. Models are quite accurate outside of the region where CFC-12 is destroyed. Figure 7.13 shows the retrieved values for CFC-12 and the relative difference to CLaMS data. In the stable region, the differences of absolute values are below 5%, which is a huge improvement in comparison to ESSenCe (Section 5.4).

## Analysis of retrieval resolution

Diagnostic values were created for the area where stable results are expected. For comparison, parts of the atmosphere outside of this area were also included. The resolution shows the size above which atmospheric structures can be discerned and is defined as the half-width full-max of the averaging kernel function of a atmospheric point. In the vertical direction, the minimum resolution is limited by the field of view of the GLORIA detector pixels. The retrieval achieves a vertical resolution of 200 m, which is consistent with the instrument design and the 1-D retrievals for ESSenCe. The vertical measurement grid is fixed by the field

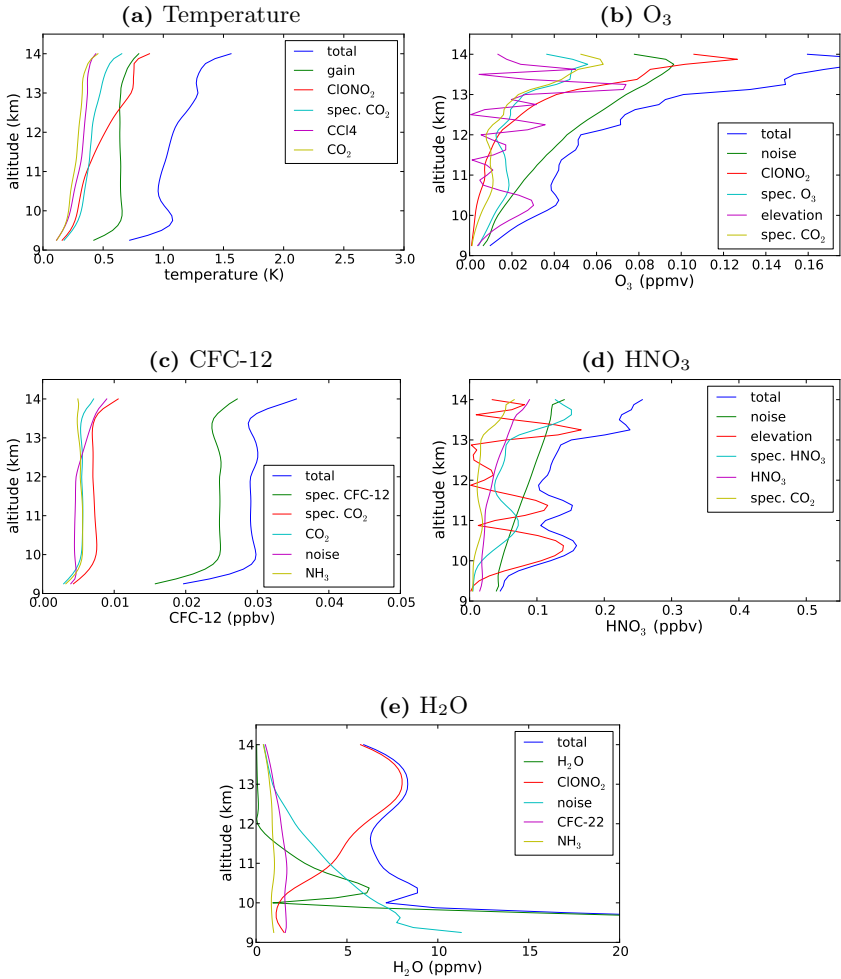
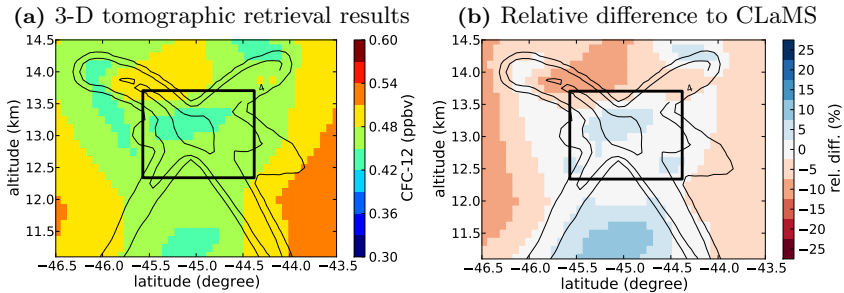
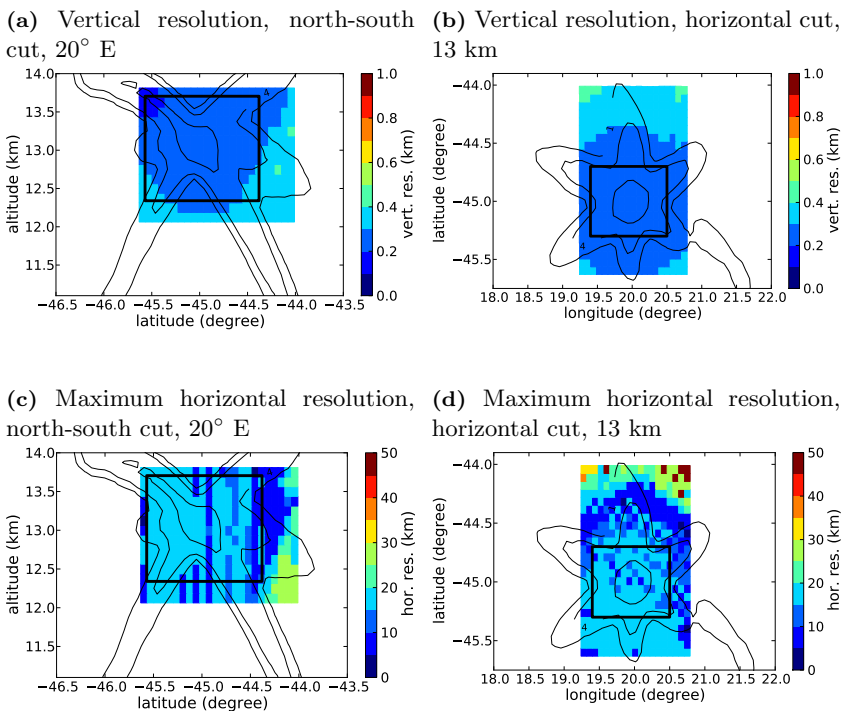


Figure 7.12: ESMVal hexagon: Error analysis for profile 175



**Figure 7.13:** Retrieval results for CFC-12 and comparison to CLaMS

of view of the detector. For the horizontal resolution the maximum from the longitudinal and latitudinal directions is taken. In 1-D retrievals, the resolution along the line of sight is 200 to 300 km. When using the same measurements in a 3-D tomographic retrieval, the horizontal resolution is dramatically improved. In the stable region, the horizontal resolution of nitric acid and ozone is  $\approx 20$  km (Figure 7.14 and 7.15). Outside of the region of tangent points, the resolution quickly becomes worse. Additionally, the centre of the averaging kernel function is no longer located at the target point but shifted towards the centre of the hexagon. This means that the information in this point is extrapolated from a region with better measurement coverage.



**Figure 7.14:** Diagnostic values for ozone. Thick black lines show the stable region derived from the tangent point density (thin black lines).

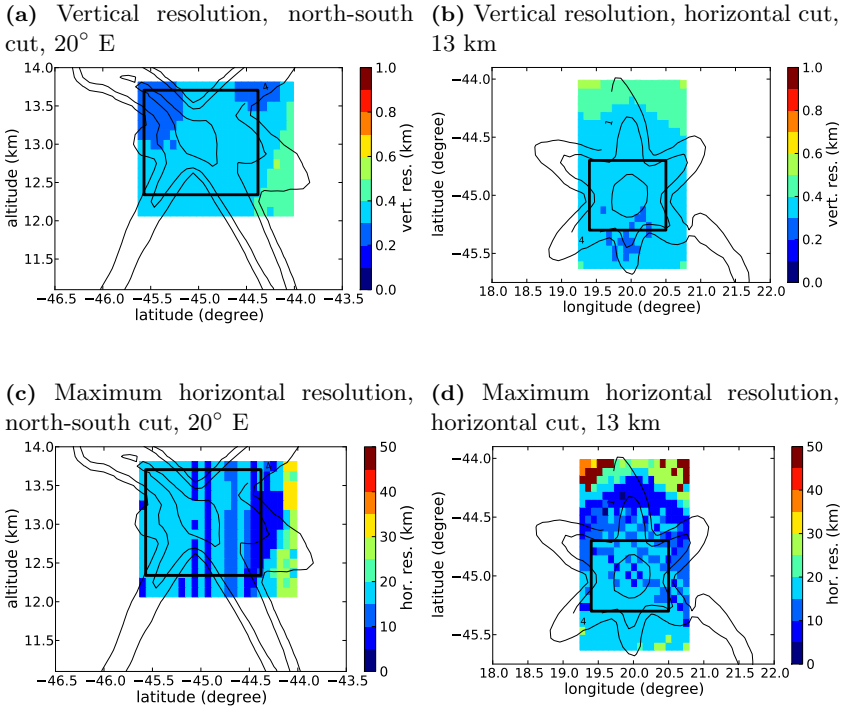


**Figure 7.15:** Diagnostic values for nitric acid. Thick black lines show the stable region derived from the tangent point density (thin black lines).

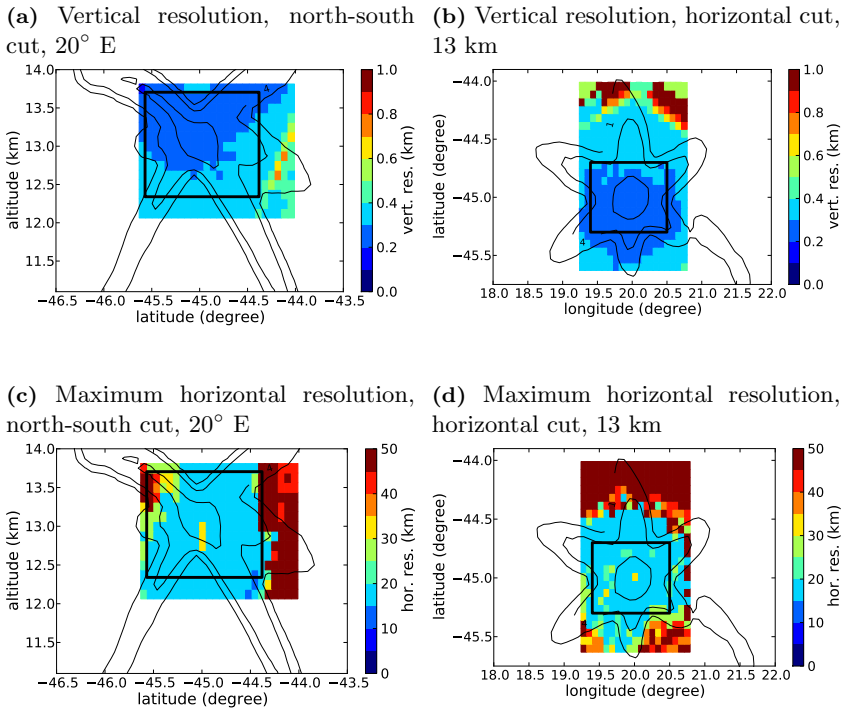


**Figure 7.16:** Diagnostic values for temperature. Thick black lines show the stable region derived from the tangent point density (thin black lines).

## Comparison with 1-D retrievals

Inhomogeneities along the line of sight are smoothed out in 1-D retrievals and can considerably modify the retrieval result for measurements of the same air mass from different angles. To show the influence of smoothing, 1-D retrievals were executed with the same microwindows and a priori data. Figures 7.17a to 7.17f show side-by-side comparisons of the 1-D retrievals and the data from 3-D retrievals sampled at the respective tangent points.

In  $\text{HNO}_3$  and  $\text{O}_3$  the structures are clearly replicated between 1-D and 3-D retrievals. At 12 km, the tangent points cross the circular artefact described in 7.3. Clear differences are visible in the water vapour at the lower altitudes. Although the structures have fewer artefacts due to vertical regularisation than in the 1-D case, values of more than 14 ppm water vapour in the lower stratosphere are unrealistic.

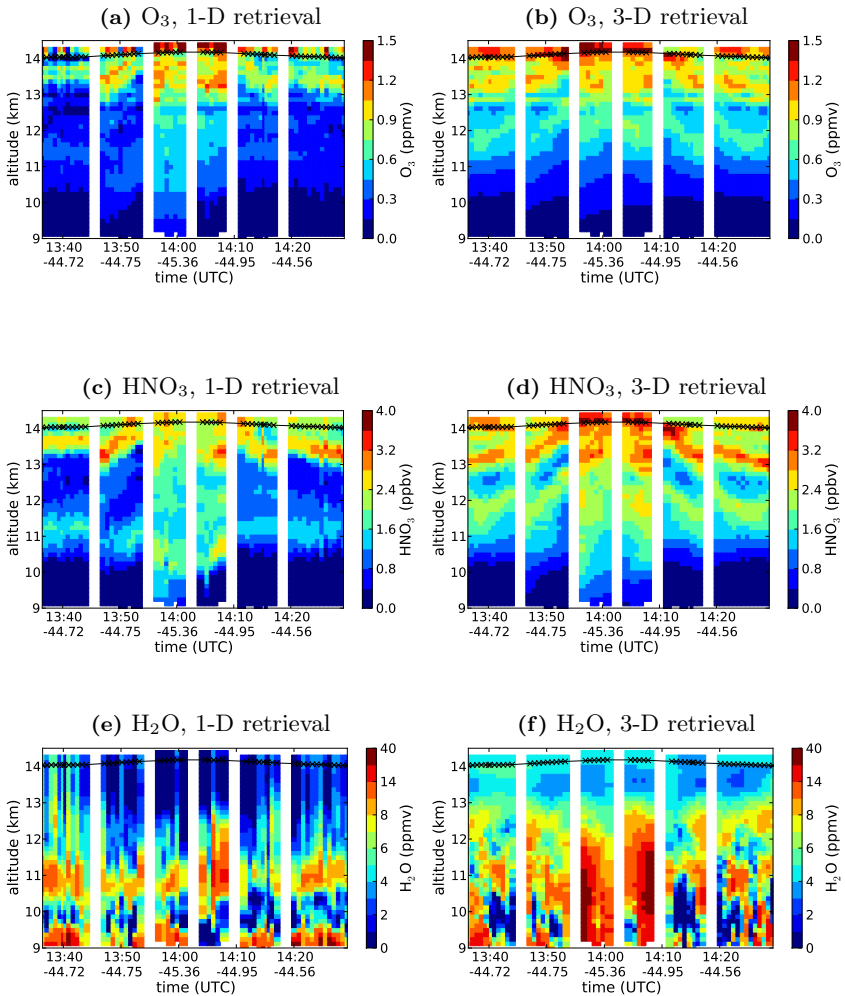


**Figure 7.17:** Comparisons between 1-D retrievals and 3-D retrievals sampled at the tangent points. The stable region in the 3-D tomographic retrieval starts at 12.5 km altitude. Altitudes below this may contain additional smoothing errors. The quality of water vapour is low, because only weak lines were used for the retrieval.

## 8. Conclusion

The ESSenCe campaign was the first practical test of the GLORIA instrument. Although it was only possible to acquire usable data during part of the flights, the campaign was still a great success.

GLORIA worked nearly flawlessly and provided a wealth of data during the following campaigns (TACTS and ESMVal). Nearly 90 hours of measurements are now available for analysis, including data from three hexagonal flight patterns.

In preparation for ESSenCe, a method for the selection and evaluation of appropriate spectral windows was developed. This algorithm was applied to the evaluation of ESSenCe and for the first multi-target 3-D tomographic retrieval with data from the ESMVal campaign.

Using the data from ESSenCe, it was possible to show the presence of a very thin filament of stratospheric air that could not be properly reproduced by other instruments. Although the results contained some biases (about 10%), the unique features of GLORIA could be demonstrated. For the important trace gases  $O_3$  and  $HNO_3$  a vertical resolution of 400 m was achieved. Temperature was derived with a vertical resolution of 1 km. The high temporal sampling made it possible to use horizontal regularisation to considerably reduce the influence of noise.

To facilitate the evaluation of large 3-D tomographic retrievals, our retrieval tool set JURASSIC was enhanced with a new parallelisation scheme. It is now possible to perform retrievals which span multiple compute nodes. The performance was increased over 70-fold in comparison to the runtime on a single node.

A first 3-D tomographic retrieval with real measurement data was done after the TACTS/ESMVal campaigns. In addition to being the first application of this method to real measurements from a hexagonal flight pattern, it extends previous simulation studies to multi-target retrievals.

We were able to show the presence of a small intrusion of stratospheric air in the observed air volume. One of the main reasons for performing 3-D tomographic retrievals is to improve spatial resolution along the line of sight, a traditional weakness of limb sounding. The horizontal resolution is about 20 km in all horizontal directions for  $O_3$  and  $HNO_3$ , in contrast to the 300 km along line of sight resolution in 1-D retrievals. For temperature the resolution is slightly worse, matching the less pronounced structures of temperature. The vertical resolution is about 300 m for all targets, which is comparable with conventional 1-D retrievals.

The results obtained in the campaigns described in this work show quite impressively the improvements that GLORIA offers in comparison to other limb sounding concept. We were able to produce high-quality profiles from the measurements in a very short time. In addition to the data generated in 1-D retrievals with a vertical resolution of 300 m or better, the 3-D tomographic technique allows the accurate reconstruction of three dimensional features in the atmosphere, increasing our knowledge of small scale dynamic processes in the UTLS region.

# A. List of Abbreviations

CLaMS	Chemical Lagrangian Model of the Stratosphere
CRISTA(-NF)	CRyogenic Infrared Spectrometers and Telescopes for the Atmosphere (- New Frontiers)
ECMWF	European Centre for Medium-Range Weather Forecasts
EGA	emissivity growth approximation
ESA	European Space Agency
ESMVal	Earth System Model Validation
ESSenCe	ESA Sounder Campaign
Envisat	Environmental Satellite
FOV	field of view
FTS	Fourier transform spectrometer
GA	genetic algorithm
GLORIA	Gimballed Limb Observer for Radiance Imaging of the Atmosphere
HAGAR	High Altitude Gas Analyzer
HIRDLS	High Resolution Dynamics Limb Sounder
IEK	Institute of Energy and Climate Research
ILS	instrument line shape
IMK	Institute for Meteorology and Climate Research
ISW	integrated spectral window
JURASSIC	JUelich RAPid Spectral SIMulation Code
LOS	Line of Sight
MARSCHALS	Millimeter-Wave Airborne Receivers for Spectroscopic Characterisation in Atmospheric Limb Sounding
MIPAS	Michelson Interferometer for Passive Atmospheric Sounding
MLS	Microwave Limb Sounder

MPI	Message Passing Interface
NASA	National Aeronautics and Space Administration
NAT	nitric acid trihydrate
NUMA	non-uniform memory access
PAN	peroxyacetyl nitrate
PREMIER	PRocess Exploration through Measurements of Infrared and millimetre-wave Emitted Radiation
SIMD	single instruction multiple data
SSE	Streaming SIMD Extensions
STCE	Software and Tools for Computational Engineering
TACTS	Transport and Composition in the UT/LMS
UTLS	upper troposphere/lower(most) stratosphere
WAS	Whole Air Sampler

## B. Mathematical Notation

In this work, real values, integer values, and functions mapping into  $\mathbb{R}$  are set in regular cursive font (e.g.  $J$ ). For vectors and vector-valued functions, a bold cursive font (e.g.  $\mathbf{x}$ ) is used. Bold regular symbols (e.g.  $\mathbf{S}$ ) refer to matrices and matrix-valued functions.

The following table list the most important mathematical symbols:

$E_{\mathbf{S}}$	The entropy of matrix $\mathbf{S}$ : $E_{\mathbf{S}} = -\frac{1}{2} \log_2(\det(\mathbf{S}))$
$F(\mathbf{x})$	The forward model: maps an atmospheric state on a measurement vector
$\mathbf{F}'(\mathbf{x})$	Jacobian matrix of the forward model
$\mathbf{F}''(\mathbf{x})$	Hessian matrix of the forward model
$H$	The information gain: $H = E_{\mathbf{S}_1} - E_{\mathbf{S}_2}$
$J(\mathbf{x})$	The cost function: $J(\mathbf{x}) = \ \mathbf{F}(\mathbf{x}) - y\ _{\mathbf{S}_\epsilon^{-1}} + \ \mathbf{x} - x_a\ _{\mathbf{S}_a^{-1}}$
$\mathbf{S}_a, \mathbf{S}_a^{-1}$	A covariance matrix of the a priori and its inverse, an a-priori precision matrix
$\mathbf{S}_\epsilon, \mathbf{S}_\epsilon^{-1}$	A measurement covariance matrix and its inverse, a measurement precision matrix
$\mathbf{S}_x, \mathbf{S}_x^{-1}$	A retrieval error covariance matrix and its inverse, a retrieval precision matrix
$\mathbf{x}$	A vector representing an atmospheric state
$\hat{\mathbf{x}}$	A vector representing an average atmospheric state
$\mathbf{y}$	A vector representing measurements

## C. Line-by-Line Calculations

This appendix provides a short overview of line-by-line calculations of radiative transfer equations based on the HITRAN (*Rothman et al.*, 2009) database. The following equations were derived from first principles to obtain an independent implementation of the radiative model needed to calculate tables for the fast JURASSIC Forward Model. It contains no optimisations and works only for homogeneous gas cells containing one emitter. The gas is assumed to be in local thermal equilibrium. Pressure and temperature is assumed to be at atmospheric levels. Table C.1 contains a list of all parameters and physical constants used and their respective sources.

The HITRAN database is a collection of spectral lines for various molecules. The most important parameters are the line strength  $S$  and the transition wavenumber  $\nu$ . The line position is shifted under pressure:

$$l_\nu = \nu + \frac{p}{p'} \delta_{\text{air}} \quad (\text{C.1})$$

The causes and effects of line broadening change depending on pressure. If the partial pressure  $p_{\text{Mol}}$  of the molecule is high, self-broadening occurs. This effect is negligible for trace gases on Earth, but is significant in other situation, e.g. for more abundant gases like  $\text{O}_2$  and  $\text{N}_2$  on Earth in other spectral ranges or  $\text{CO}_2$  on Mars.

$$p_{\text{Mol}} = \text{vmr} \cdot p \quad (\text{C.2a})$$

$$\gamma = (\gamma_{\text{air}} \cdot (p - p_{\text{Mol}}) + \gamma_{\text{self}} \cdot p_{\text{Mol}}) \cdot p^{-1} \quad (\text{C.2b})$$

The two most important causes for line broadening are Lorentz broadening, which is dominant at higher pressures ( $> 100$  hPa), and Doppler

Input parameters		
Mol	Molecular number	Molecule in HITRAN
vmr	Volume mixing ratio	ppv
$p$	Pressure	hPa
$T$	Temperature	K
$f$	Wavenumber to be evaluated	$\text{cm}^{-1}$
$d$	Length of the cell	cm
Supplied by HITRAN		
$\nu$	Vacuum transition wavenumber	$\text{cm}^{-1}$
$\delta_{\text{air}}$	Pressure shift	$\text{cm}^{-1}\text{atm}^{-1}$
$\gamma_{\text{self}}$	Self-broadened half-width	$\text{cm}^{-1}\text{atm}^{-1}$
$\gamma_{\text{air}}$	Air-broadened half-width	$\text{cm}^{-1}\text{atm}^{-1}$
$n_{\text{air}}$	Temperature dependence exponent of $\gamma_{\text{air}}$	Unitless
$m_{\text{Mol}}$	Molar mass	g
$E''$	Lower energy state	$\text{cm}^{-1}$
$Q_{\text{tot}}$	Total internal partition sum (TIPS)	Unitless
$T'$	HITRAN standard temperature	K
$p'$	HITRAN standard pressure	hPa
$S(T')$	Intensity, line strength	$\text{cm}^{-1}/(\text{molecule cm}^{-2})$
Constants		
$k_B$	Boltzmann constant	$\text{J K}^{-1}$
$c$	Speed of light	$\text{cm s}^{-1}$
$c_1$	First radiation constant	$\text{W m}^2 \text{sr}^{-1}$
$c_2$	Second radiation constant	m K

**Table C.1:** Values used for line-by-line calculations

broadening at lower pressure. The half-width of both can be calculated according to *Petty* (2006):

$$\gamma_L = \gamma \frac{p}{p'} \cdot \left( \frac{T'}{T} \right)^{n_{\text{air}}} \quad (\text{C.3a})$$

$$\gamma_D = \sqrt{\frac{2k_{\text{B}}T \ln(2)}{m_{\text{Mol}}c^2}} l_{\nu} \quad (\text{C.3b})$$

Line strength in HITRAN is normalised to  $T' = 296$  K. Appropriate scaling must be applied to calculate the strength for temperature  $T$  (*Šimečková et al.*, 2006). The quotient of the total internal partition sums is supplied by the algorithm included in HITRAN. The TIPS numbers describe the proportions of molecules in different excited states and are only valid in local thermal equilibrium.

$$S(T) = S(T') \frac{Q_{\text{tot}}(T')}{Q_{\text{tot}}(T)} \frac{e^{E''c_2/T'}}{e^{E''c_2/T}} \left( \frac{1 - e^{-c_2\nu/T}}{1 - e^{-c_2\nu/T'}} \right) \quad (\text{C.4})$$

By applying a line shape function, we obtain the intensity at  $f$ . The Voigt profile  $V$  is usually a sufficient approximation for the stratosphere (*Kuntz*, 1997):

$$S(f) = V(f, l_{\nu}, \gamma_L, \gamma_D) \cdot S(T) \quad (\text{C.5})$$

From this, we can calculate the optical path depth  $\tau$  and the emissivity  $\epsilon$ :

$$\tau(f) = S(f) \cdot d \cdot \left( \frac{p}{10^4 k_{\text{B}} T} \right) \cdot \text{vmr} \quad (\text{C.6a})$$

$$\epsilon(f) = 1 - e^{-\tau(f)} \quad (\text{C.6b})$$

Emissivities are calculated on a very fine spectral grid ( $0.0005 \text{ cm}^{-1}$ ). For each sample, all lines with a transition wavenumber within  $25 \text{ cm}^{-1}$  are considered and their optical paths added together to adequately account for the line width. In a complete line-by-line calculation, emissions from other emitters are considered by adding them. Special care was taken to apply correct physical units and the source code was annotated with all conversions.

## D. Adjoint Mode

Algorithmic differentiation is a powerful tool to calculate derivatives of some computer-implemented functions. It works by repeatedly applying the chain rule to atomic functions. Here, an atom is a function of which the derivatives can be trivially calculated (basic arithmetic operations, but also log, exp, pow). The derivative is either calculated along with the calculation in *forward mode* or by storing all partial derivatives on a tape and replaying it backwards. The latter is called *adjoint mode* and is used in JURASSIC. The *adjoint mode* can be used to calculate a single row of the Jacobian matrix, whereas the *forward mode* can recover a column.

The working principle of the adjoint mode is shown in Figure D.1. While calculating the value of  $r = f(x, y, z) = x \cdot (y + z)$  we store the partial derivatives  $\frac{\partial b}{\partial x}$ ,  $\frac{\partial b}{\partial a}$ ,  $\frac{\partial a}{\partial y}$  and  $\frac{\partial a}{\partial z}$  on the tape, a memory structure optimised for this task. We can recover the derivative and in this case the Jacobian matrix by playing the tape backwards and using only multiply and add operations. If the function returns a vector instead of a scalar, we have to repeat this for each vector element to recover the complete Jacobian matrix.

In JURASSIC, each element of the result vector represents exactly one integrated spectral window of one pencil beam, which can be calculated independently of all others; thus we only need to store the tape for the calculation of one pencil beam. The adjoint mode is implemented by using the C++ operator overloading feature. A class *active* with similar semantics as the basic in-built type *double* is used in all operations which influence the derivative. This is trivially defined by the data flow. A *double* can affect the value of *active*, but an *active* variable can never affect the value a *double*.

To achieve optimal performance the tape should be as small as possible. Recording a tape generates a series of Jacobian matrices that must be

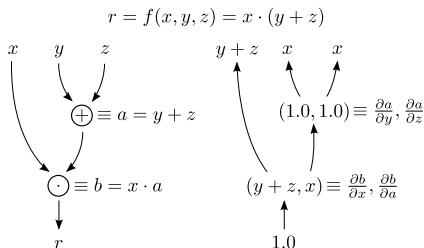


**Figure D.1:** Adjoint derivation for a simple function. Left: Forward mode records Jacobian matrix of atomic operations. Right: Backward replay by repeated multiplication of Jacobian matrices.

multiplied together. One way to reduce the tape size is to pre-multiply the derivatives of some operations, if this yields a matrix with fewer entries. In general, this problem is computationally hard (Naumann, 2008), but in the case of statement compression it is always beneficial to do so. We define a statement as the sequence of atomic functions that are assigned to a variable by the overloaded  $C++=$ -operator. Taking the example from Figure D.1: four values need to be stored on the tape. When we store these four values on a temporary tape and use them to calculate  $\frac{\partial x}{\partial r}$ ,  $\frac{\partial y}{\partial r}$  and  $\frac{\partial z}{\partial r}$  at the time of the assignment, only three values need to be stored on the global tape. Storing values on a small temporary tape is usually faster as this tape can be kept in the processor cache in contrast to the large global tape.



## Acknowledgments

I would like to thank Prof. Dr. Martin Riese for providing me with the opportunity to work in this field.

Special thanks to Dr. Martin Kaufmann for always motivating me whenever needed.

My thanks go to my colleagues Dr. Jörn Ungermann and Tobias Guggenmoser. Without their contributions this thesis would not have been possible.

I would also like to thank the whole GLORIA team for their amazing work on the instrument.

I am grateful to everyone involved in the ESSenCe campaign for their successful work. I would like to make special mention of Anne Kleinert for providing the first calibrated GLORIA measurements.

Thanks to the TACTS and ESMVal teams for the flawless campaigns and especially to Peter Preusse, Andreas Ebersoldt and Christian Sartorius for the time in Cyprus.

I would like to thank the CLaMS team for the data used in the planning and evaluation of GLORIA missions.

I am grateful to all my colleagues at IEK-7 and the University of Wuppertal. It was a pleasure to work with them. Special thanks to the past and present attendees of the secret coffee break, who made my live in Jülich so much more enjoyable.

Finally, I would like to thank my parents for their unconditional support.

# Bibliography

- Bacmeister, J. T., V. Kuell, D. Offermann, M. Riese, and J. W. Elkins (1999), Intercomparison of satellite and aircraft observations of ozone, CFC-11, and NO<sub>y</sub> using trajectory mapping, *Journal of Geophysical Research: Atmospheres (1984–2012)*, 104(D13), 16,379–16,390.
- Bai, Z. (2000), *Templates for the solution of algebraic eigenvalue problems: a practical guide*, vol. 11, Siam.
- Bradshaw, N., G. Vaughan, R. Busen, S. Garcelon, R. Jones, T. Gardiner, and J. Hacker (2002), Tracer filamentation generated by small-scale rossby wave breaking in the lower stratosphere, *Journal of Geophysical Research: Atmospheres (1984–2012)*, 107(D23), ACL–12.
- Brault, J. W. (1996), New approach to high-precision fourier transform spectrometer design, *Applied Optics*, 35(16), 2891–2896, doi:10.1364/AO.35.002891.
- Dee, D. P., S. M. Uppala, A. J. Simmons, P. Berrisford, P. Poli, S. Kobayashi, U. Andrae, M. A. Balmaseda, G. Balsamo, P. Bauer, P. Bechtold, A. C. M. Beljaars, L. van de Berg, J. Bidlot, N. Bormann, C. Delsol, R. Dragani, M. Fuentes, A. J. Geer, L. Haimberger, S. B. Healy, H. Hersbach, E. V. Hólm, L. Isaksen, P. Kållberg, M. Köhler, M. Matricardi, A. P. McNally, B. M. Monge-Sanz, J.-J. Morcrette, B.-K. Park, C. Peubey, P. de Rosnay, C. Tavolato, J.-N. Thépaut, and F. Vitart (2011), The ERA-Interim reanalysis: configuration and performance of the data assimilation system, *Quarterly Journal of the Royal Meteorological Society*, 137(656), 553–597, doi:10.1002/qj.828.
- Dudhia, A. (2000), Michelson Interferometer for Passive Atmospheric

- Sounding (MIPAS) Reference Forward Model (RFM). Software User's Manual.
- Dudhia, A., V. L. Jay, and C. D. Rodgers (2002), Microwindow selection for high-spectral-resolution sounders, *Applied Optics*, *41*(18), 3665, doi:10.1364/AO.41.003665.
- Engel, A., and H. Boenisch (2013), An overview on the TACTS mission using the new German research aircraft HALO in summer 2012, in *EGU General Assembly Conference Abstracts*, vol. 15, p. 9191.
- Engl, H. W., M. Hanke, and A. Neubauer (1996), *Regularization of inverse problems*, vol. 375, Springer.
- Fellgett, P. B. (1951), The multiplex advantage, Ph.D. thesis, University of Cambridge, Cambridge, UK.
- Fischer, H., M. Birk, C. Blom, B. Carli, M. Carlotti, T. v. Clarmann, L. Delbouille, A. Dudhia, D. Ehnhalt, M. Endemann, et al. (2007), MIPAS: an instrument for atmospheric and climate research, *Atmospheric Chemistry and Physics Discussions*, *7*(3), 8795–8893.
- Friedl-Vallon, F., M. Riese, G. Maucher, A. Lengel, F. Hase, P. Preusse, and R. Spang (2006), Instrument concept and preliminary performance analysis of GLORIA, *Advances in Space Research*, *37*(12), 2287–2291.
- Garcia, R. R., D. R. Marsh, D. E. Kinnison, B. A. Boville, and F. Sassi (2007), Simulation of secular trends in the middle atmosphere, 1950–2003, *Journal of Geophysical Research*, *112*, doi:10.1029/2006JD007485.
- Gordley, L. L., and J. M. Russell III (1981), Rapid inversion of limb radiance data using an emissivity growth approximation, *Applied Optics*, *20*(5), 807, doi:10.1364/AO.20.000807.
- Groß, J.-U., G. Günther, P. Konopka, R. Müller, D. McKenna, F. Stroh, B. Vogel, A. Engel, M. Müller, K. Hoppel, et al. (2002), Simulation of ozone depletion in spring 2000 with the Chemical Lagrangian Model of the Stratosphere (CLaMS), *Journal of Geophysical Research: Atmospheres (1984–2012)*, *107*(D20), SOL–38.

- Grossmann, K. U., D. Offermann, O. Gusev, J. Oberheide, M. Riese, and R. Spang (2002), The CRISTA-2 mission, *J. Geophys. Res.*, *107*, D23, doi:10.1029/2001JD000667.
- Hadamard, J. (1902), Sur les problèmes aux dérivées partielles et leur signification physique, *Princeton University Bull.*, pp. 49–52.
- Hoffmann, L., M. Ern, M. Kaufmann, P. Preuße, R. Spang, and M. Riese (2005a), Retrieval of atmospheric trace constituents from Envisat MIPAS observations by means of rapid radiative transfer calculations: First results for CFC-11, in *Envisat & ERS Symposium*, vol. 572, p. 225.
- Hoffmann, L., R. Spang, M. Kaufmann, and M. Riese (2005b), Retrieval of CFC-11 and CFC-12 from Envisat MIPAS observations by means of rapid radiative transfer calculations, *Advances in Space Research*, *36*, 915–921.
- Holton, J. R., P. H. Haynes, M. E. McIntyre, A. R. Douglass, R. B. Rood, and L. Pfister (1995), Stratosphere-troposphere exchange, *Rev. Geophys.*, *33*, 403–439.
- Höpfner, M., C. Blom, T. von Clarmann, H. Fischer, N. Glatthor, T. Gulde, F. Hase, C. Keim, W. Kimmig, K. Lessenich, et al. (2000), MIPAS–STR data analysis of APE–GAIA measurements, in *Proceedings of the International Radiation Symposium IRS*.
- Householder, A. (1975), *The theory of matrices in numerical analysis*, New York: Dover Publications.
- Jacquinet, P. (1960), New developments in interference spectroscopy, *Reports on progress in physics*, *23*(1), 267.
- Kalicinsky, C., J.-U. Groöß, G. Günther, J. Ungermann, J. Blank, S. Höfer, L. Hoffmann, P. Knieling, F. Olschewski, R. Spang, et al. (2013), Small-scale transport structures in the arctic winter 2009/2010, *Atmospheric Chemistry and Physics Discussions*, *13*(4), 10,463–10,498.
- Kaufmann, M., J. Blank, F. Friedl-Vallon, D. Gerber, T. Guggenmoser, M. Hoepfner, A. Kleinert, M. K. Sha, H. Oelhaf, M. Riese,

- O. Suminska-Ebersoldt, W. Woiwode, R. Sid-dans, B. Kerridge, B. Moyna, S. Rea, and M. Oldfield (2013), Technical assistance for the deployment of airborne limb-sounders during ESSenCe, *Tech. rep.*, Forschungszentrum Jülich GmbH.
- Kullback, S., and R. A. Leibler (1951), On information and sufficiency, *The Annals of Mathematical Statistics*, 22(1), 79–86, doi:10.1214/aoms/1177729694.
- Kullmann, A., M. Riese, F. Olschewski, F. Stroh, and K. U. Grossmann (2004), Cryogenic Infrared Spectrometers and Telescopes for the Atmosphere - New Frontiers, in *Proc. SPIE*, vol. 5570, pp. 423–432, doi:10.1117/12.564856.
- Kuntz, M. (1997), A new implementation of the Humlicek algorithm for the calculation of the Voigt profile function, *Journal of Quantitative Spectroscopy and Radiative Transfer*, 57(6), 819 – 824, doi:10.1016/S0022-4073(96)00162-8.
- Lotz, J., U. Naumann, and J. Ungermann (2011), Efficient discrete adjoint computation in a spectral simulation code, *Tech. Rep. AIB-2011-05*, RWTH Aachen and Forschungszentrum Jülich.
- Marquardt, D. W. (1963), An algorithm for least-squares estimation of nonlinear parameters, *SIAM Journal on Applied Mathematics*, 11(2), 431–441.
- Michelson, A. A., and E. W. Morley (1887), On the relative motion of the earth and of the luminiferous ether, *Sidereal Messenger*, 6, 306–310.
- Mitchell, M. (1998), *An Introduction to Genetic Algorithms (Complex Adaptive Systems)*, A Bradford Book.
- Naumann, U. (2008), Optimal Jacobian accumulation is NP-complete, *Mathematical Programming*, 112(2), 427–441, doi:10.1007/s10107-006-0042-z.
- Nocedal, J., and S. J. Wright (2006), *Numerical Optimization*, Springer, New York.

- Nolet, G. (1985), Solving or resolving inadequate and noisy tomographic systems, *J. Comput. Phys.*, *61*(3), 463–482, doi:10.1016/0021-9991(85)90075-0.
- Norton, R. H., and R. Beer (1976), New apodizing functions for Fourier spectrometry, *Journal of the Optical Society of America*, *66*(3), 259, doi:10.1364/JOSA.66.000259.
- Offermann, D., K.-U. Grossmann, P. Barthol, P. Knieling, M. Riese, and R. Trant (1999), Cryogenic Infrared Spectrometers and Telescopes for the Atmosphere (CRISTA) experiment and middle atmosphere variability, *J. Geophys. Res.*, *104*, 16,311–16,325, doi:10.1029/1998JD100047.
- Olschewski, F., C. Rolf, P. Steffens, A. Kleinert, C. Piesch, A. Ebersoldt, C. Monte, B. Gutschwager, J. Hollandt, P. Preusse, et al. (2012), In-flight blackbody calibration sources for the GLORIA interferometer, in *SPIE Optical Engineering+ Applications*, pp. 85,110I–85,110I, International Society for Optics and Photonics.
- Petty, G. (2006), *A first course in atmospheric radiation*, Sundog Publishing.
- Plumb, R. A. (1992), Rossby wave breaking, microbreaking, filamentation and secondary vortex formation: The dynamics of a perturbed vortex, *Journal of the Atmospheric Sciences*, *49*, 462–476.
- Radon, J. (1917), Über die Bestimmung von Funktionen durch ihre Integralwerte längs gewisser Mannigfaltigkeiten, *Berichte über die Verhandlungen der Königlich-Sächsischen Gesellschaft der Wissenschaften zu Leipzig, Mathematisch-Physische Klasse*, *69*, 262–277.
- Read, W., A. Lambert, J. Bacmeister, R. Cofield, L. Christensen, D. Cuddy, W. Daffer, B. Drouin, E. Fetzer, L. Froidevaux, et al. (2007), Aura Microwave Limb Sounder upper tropospheric and lower stratospheric H<sub>2</sub>O and relative humidity with respect to ice validation, *Journal of Geophysical Research*, *112*(D24), D24S35.
- Remedios, J. J., R. J. Leigh, A. M. Waterfall, D. P. Moore, H. Semblhi, I. Parkes, J. Greenhough, M. Chipperfield, and D. Hauglustaine (2007), MIPAS reference atmospheres and comparisons to

- V4.61/V4.62 MIPAS level 2 geophysical data sets, *Atmospheric Chemistry and Physics Discussions*, 7(4), 9973–10,017, doi:10.5194/acpd-7-9973-2007.
- Riese, M., P. Preusse, R. Spang, M. Ern, M. Jarisch, U. Grossmann, and D. Offermann (1997), Measurements of trace gases by the cryogenic infrared spectrometers and telescopes for the atmosphere CRISTA experiment, *Adv. Space Res.*, 19, 563–566, doi:10.1016/S0273-1177(97)00172-5.
- Riese, M., R. Spang, P. Preusse, M. Ern, M. Jarisch, D. Offermann, and K. U. Grossmann (1999), Cryogenic Infrared Spectrometers and Telescopes for the Atmosphere (CRISTA) data processing and atmospheric temperature and trace gas retrieval, *J. Geophys. Res.*, 104, 16,349–16,367, doi:10.1016/S0273-1177(97)00172-5.
- Riese, M., F. Friedl-Vallon, R. Spang, P. Preusse, C. Schiller, L. Hoffmann, P. Konopka, H. Oelhaf, T. von Clarmann, and M. Höpfner (2005), GLOBal limb Radiance Imager for the Atmosphere (GLORIA): Scientific objectives, *Adv. Space Res.*, 36, 989–995, doi:10.1016/j.asr.2005.04.115.
- Riese, M., F. Ploeger, A. Rap, B. Vogel, P. Konopka, M. Dameris, , and P. Forster (2012), Impact of uncertainties in atmospheric mixing on simulated UTLS composition and related radiative effects, *J. Geophys. Res.*, 117, D16,305, doi:10.1029/2012JD017751.
- Rodgers, C. D. (2000), *Inverse Methods for Atmospheric Sounding: Theory and Practice, Series on Atmospheric, Oceanic and Planetary Physics*, vol. 2, World Scientific, Singapore.
- Rothman, L., I. Gordon, A. Barbe, D. Benner, P. Bernath, M. Birk, V. Boudon, L. Brown, A. Campargue, J.-P. Champion, K. Chance, L. Coudert, V. Dana, V. Devi, S. Fally, J.-M. Flaud, R. Gamache, A. Goldman, D. Jacquemart, I. Kleiner, N. Lacome, W. Lafferty, J.-Y. Mandin, S. Massie, S. Mikhailenko, C. Miller, N. Moazzen-Ahmadi, O. Naumenko, A. Nikitin, J. Orphal, V. Perevalov, A. Perrin, A. Predoi-Cross, C. Rinsland, M. Rotger, M. Simecková, M. Smith, K. Sung, S. Tashkun, J. Tennyson, R. Toth, A. Vandaele, and J. V. Auwera (2009), The HITRAN 2008 molecular spectroscopic database,

- Journal of Quantitative Spectroscopy and Radiative Transfer*, 110(9-10), 533–572, doi:10.1016/j.jqsrt.2009.02.013.
- Sawamura, P., J. P. Vernier, J. E. Barnes, T. A. Berkoff, E. J. Welton, L. Alados-Arboledas, F. Navas-Guzmán, G. Pappalardo, L. Mona, F. Madonna, D. Lange, M. Sicard, S. Godin-Beekmann, G. Payen, Z. Wang, S. Hu, S. N. Tripathi, C. Cordoba-Jabonero, and R. M. Hoff (2012), Stratospheric AOD after the 2011 eruption of Nabro volcano measured by lidars over the Northern Hemisphere, *Environmental Research Letters*, 7(3), 034013, doi:10.1088/1748-9326/7/3/034013.
- Schlager, H., V. Eyring, et al. (2013), HALO airborne pole-to-pole measurements of trace gases in the Atlantic and Indian Oceans for Earth System Model validation, in *EGU General Assembly Conference Abstracts*, vol. 15, p. 12030.
- Shannon, C. E. (1948), A mathematical theory of communication, *Bell System Technical Journal*, 27, 379–423.
- Spang, R., J. J. Remedios, and M. P. Barkley (2004), Colour indices for the detection and differentiation of cloud type in infra-red limb emission spectra, *Adv. Space Res.*, 33, 1041–1047, doi:10.1016/S0273-1177(03)00585-4.
- Sutter, H. (2005), The free lunch is over: A fundamental turn toward concurrency in software, *Dr. Dobbs's Journal*, 30(3), 202–210.
- Tarantola, A. (2004), *Inverse Problem Theory*, 111ff pp., Society for Industrial and Applied Mathematics, Philadelphia.
- Tikhonov, A. N., and V. Y. Arsenin (1977), *Solutions of ill-posed problems*, Winston, Washington D.C., USA.
- Twomey, S. (1977), *Introduction to the Mathematics of Inversion in Remote Sensing and Indirect Measurements*, Dover Publications.
- Ungermann, J. (2011), *Tomographic reconstruction of atmospheric volumes from infrared limb-imager measurements*, vol. 106, Forschungszentrum Jülich.

- Ungermann, J. (2013), Improving retrieval quality for airborne limb-sounders by horizontal regularisation, *Atmos. Meas. Tech.*, *6*(1), 15–32, doi:10.5194/amt-6-15-2013.
- Ungermann, J., L. Hoffmann, P. Preusse, M. Kaufmann, and M. Riese (2010a), Tomographic retrieval approach for mesoscale gravity wave observations by the PREMIER infrared limb-sounder, *Atmos. Meas. Tech.*, *3*(2), 339–354, doi:10.5194/amt-3-339-2010.
- Ungermann, J., M. Kaufmann, L. Hoffmann, P. Preusse, H. Oelhaf, F. Friedl-Vallon, and M. Riese (2010b), Towards a 3-D tomographic retrieval for the air-borne limb-imager GLORIA, *Atmos. Meas. Tech.*, *3*(6), 1647–1665, doi:10.5194/amt-3-1647-2010.
- Ungermann, J., J. Blank, J. Lotz, K. Leppkes, L. Hoffmann, T. Guggenmoser, M. Kaufmann, P. Preusse, U. Naumann, and M. Riese (2011), A 3-D tomographic retrieval approach with advection compensation for the air-borne limb-imager GLORIA, *Atmos. Meas. Tech.*, *4*(11), 2509–2529, doi:10.5194/amt-4-2509-2011.
- Ungermann, J., L. Pan, C. Kalicinsky, F. Olschewski, P. Knieling, J. Blank, T. Guggenmoser, F. Stroh, L. Hoffmann, and M. Riese (2012a), Filamentary structure in chemical tracer distributions near the subtropical jet following a wave-breaking event, *Atmos. Chem. Phys. Discuss.*, submitted.
- Ungermann, J., C. Kalicinsky, F. Olschewski, P. Knieling, L. Hoffmann, J. Blank, W. Woiwode, H. Oelhaf, E. Hösen, C. M. Volk, A. Ulanovsky, F. Ravagnani, K. Weigel, F. Stroh, and M. Riese (2012b), CRISTA-NF measurements with unprecedented vertical resolution during the REC-ONCILE aircraft campaign, *Atmos. Meas. Tech.*, *5*(5), 1173–1191, doi:10.5194/amt-5-1173-2012.
- Veldhuizen, T. (1995), Expression templates, *C++ Report*, *7*(5), 26–31.
- von Clarmann, T., and G. Echle (1998), Selection of optimized microwindows for atmospheric spectroscopy, *Applied optics*, *37*(33), 7661–7669.
- von Clarmann, T., C. De Clercq, M. Ridolfi, M. Höpfner, and J. Lambert (2009), The horizontal resolution of MIPAS, *Atmos. Meas. Techn.*, *2*, 47–54.

- von Hobe, M., S. Griefsbach, L. Hoffmann, J.-P. Vernier, M. Höpfner, F. Ploeger, C. Hoppe, R. Müller, and P. Konopka (2013), Stratospheric aerosol enhancements from the Nabro eruption in 2011: an investigation of possible transport pathways using trajectory ensembles, *Geophysical research abstracts*, 15, EGU2013–12,453.
- Weigel, K., M. Riese, L. Hoffmann, S. Hofer, C. Kalicinsky, P. Knieling, F. Olschewski, P. Preusse, F. Stroh, R. Spang, and C. M. Volk (2010), CRISTA-NF measurements during the AMMA-SCOUT-O<sub>3</sub> aircraft campaign, *Atmos. Meas. Tech.*, 3(2), 1437–1455, doi:10.5194/amt-3-1437-2010.
- Weigel, K., L. Hoffmann, G. Günther, F. Khosrawi, F. Olschewski, P. Preusse, R. Spang, F. Stroh, and M. Riese (2012), A stratospheric intrusion at the subtropical jet over the mediterranean sea: air-borne remote sensing observations and model results, *Atmospheric Chemistry and Physics*, 12(18), 8423–8438.
- Woiwode, W., H. Oelhaf, T. Gulde, C. Piesch, G. Maucher, A. Ebersoldt, C. Keim, M. Höpfner, S. Khaykin, F. Ravegnani, A. E. Ulanovsky, C. M. Volk, E. Hösen, A. Dörnbrack, J. Ungermann, C. Kalicinsky, and J. Orphal (2012), Mipas-str measurements in the arctic utls in winter/spring 2010: instrument characterization, retrieval and validation, *Atmos. Meas. Tech.*, 5(6), 1205–1228, doi:10.5194/amt-5-1205-2012.
- Šimečková, M., D. Jacquemart, L. S. Rothman, R. R. Gamache, and A. Goldman (2006), Einstein A-coefficients and statistical weights for molecular absorption transitions in the HITRAN database, *Journal of Quantitative Spectroscopy and Radiative Transfer*, 98(1), 130 – 155, doi:10.1016/j.jqsrt.2005.07.003.